

# MILLIMETER- AND SUBMILLIMETER-WAVE OBSERVATIONS OF THE OMC-2/3 REGION. III. AN EXTENSIVE SURVEY FOR MOLECULAR OUTFLOWS

SATOKO TAKAHASHI,<sup>1,2</sup> MASAO SAITO,<sup>2</sup> NAGAYOSHI OHASHI,<sup>3</sup> NOBUHIKO KUSAKABE,<sup>4</sup> SHIGEHISA TAKAKUWA,<sup>3</sup>  
 YOSHITO SHIMAJIRI,<sup>5</sup> MOTOHIDE TAMURA,<sup>4</sup> AND R. KAWABE<sup>6</sup>

*Received 2008 April 3; accepted 2008 July 30*

## ABSTRACT

Using the ASTE 10 m submillimeter telescope and the 1.4 m Infrared Survey Facility (IRSF), we performed an extensive outflow survey in the Orion Molecular Cloud 2 and 3 region. Our survey, which includes 41 potential star-forming sites, has been newly compiled using multiwavelength data based on millimeter- and submillimeter-continuum observations, as well as radio continuum observations. From the CO(3–2) observations performed with the Atacama Submillimeter Telescope Experiment (ASTE) 10 m telescope, we detected 14 CO molecular outflows, seven of which were newly identified. This higher detection rate, as compared to previous CO(1–0) results in the same region, suggests that CO(3–2) may be a better outflow tracer. Physical properties of these outflows and their possible driving sources were derived. Derived parameters were compared with those of CO outflows in low- and high-mass star-forming regions. We show that the CO outflow momentum correlates with the bolometric luminosity of the driving source and with the envelope mass, regardless of the mass of the driving sources. In addition to these CO outflows, seven sources having near-IR features suggestive of outflows were also identified.

*Subject headings:* ISM: clouds — ISM: individual (OMC-2/3) — ISM: jets and outflows — radio lines: ISM — stars: formation

## 1. INTRODUCTION

CO molecular outflows are ubiquitous phenomena in low- to high-mass star-forming regions (e.g., Bachiller & Tafalla 1999; Zhang et al. 2001; Arce et al. 2007 for reviews). This phenomenon is considered to be directly associated with the main accretion phase in protostars, and is frequently used to identify protostars in dense cores. Hence the CO outflows provide the primary information concerning the mass accretion and ejection processes during the protostellar evolution. Previous single-dish surveys revealed the physical nature of CO outflows toward hundreds of low- to high-mass young stellar objects (e.g., Cabrit & Bertout 1992; Shepherd & Churchwell 1996; Bontemps et al. 1996; Beuther et al. 2002; Zhang et al. 2001; 2005). An extensive outflow survey of low-mass objects by Bontemps et al. (1996) found that the momentum flux of the CO outflows is positively correlated with the bolometric luminosity and also positively correlated with the mass of the associated parent cores. Recent high-mass studies also show the above correlations continuing to the high-mass region over several orders of magnitude in mass and bolometric luminosity (e.g., Churchwell 1997; Beuther et al. 2002; Zhang et al. 2005). On the other hand, the systematic studies focused on outflows associated with intermediate-mass protostars ( $2 \leq M_* \leq 8 M_\odot$ ) are still limited, although several candidates have been investi-

gated in detail to date (e.g., Fuente et al. 2005; Takahashi et al. 2006; Beltran et al. 2006, 2008). Studies of the intermediate-mass outflows are important for revealing the evolution of intermediate-mass stars. But more importantly, such studies address the question of whether the same basic accretion and outflow processes operate continuously from low- to high-mass stars.

In this paper we present the results of our extensive outflow survey toward one of the nearest intermediate-mass star-forming regions: The Orion Molecular Cloud -2/3 (OMC-2/3;  $d = 450$  pc; Genzel & Stutzki 1989). The goals of this project are to (1) search for outflows in OMC-2/3 with high sensitivity and high spatial resolution, (2) combine the detected outflow results and the centimeter to mid-infrared continuum information to identify a driving source of the outflows, and (3) reveal the structures and the physical properties of each outflow. In the OMC-2/3 region, 38 millimeter and submillimeter dust continuum sources were detected (Chini et al. 1997; Lis et al. 1998; Nielbock et al. 2003). Free-free jets were also detected at 3.6 cm toward 11 of the embedded sources, and eight of 11 sources are associated with the dust continuum sources (Reipurth et al. 1999). Shock-excited H<sub>2</sub> knots, which probably trace shock fronts within each flow, are associated with these embedded sources (Yu et al. 1997; 2000; Stanke et al. 2002). Aso et al. (2000) and Williams et al. (2003) made mapping observations in the CO(1–0) emission and identified nine CO outflows. They found that the outflows in OMC-2/3 are mostly spatially compact (i.e., possess short dynamical timescales of a few  $\times 10^4$  yr), and energetic ( $\sim$ several  $\times 10^{-4} M_\odot \text{ km s}^{-1}$ ). However, previous outflow identifications have ambiguities, because the CO(1–0) emission is often significantly affected by the contamination from the ambient molecular cloud. This made it difficult to identify small and faint outflows and differentiate them from the ambient molecular gas. Furthermore, pre- and protostellar candidates in OMC-2/3 are lying along the filament within a few  $\times 0.1$  pc. The crowded core distributions also made it difficult to identify which is the driving source of each outflow.

We report results of our high-sensitivity molecular outflow survey in the submillimeter CO(3–2) emission with the ASTE

<sup>1</sup> Academia Sinica Institute of Astronomy and Astrophysics, P.O. Box 23-141, Taipei 106, Taiwan; and Department of Astronomical Science, The Graduate University for Advanced Studies, National Astronomical Observatory of Japan, Osawa 2-21-1, Mitaka, Tokyo 181-8588, Japan; satoko\_t@asiaa.sinica.edu.tw.

<sup>2</sup> ALMA Project Office, National Astronomical Observatory of Japan, Osawa 2-21-1, Mitaka, Tokyo 181-8588, Japan.

<sup>3</sup> Academia Sinica Institute of Astronomy and Astrophysics, P.O. Box 23-141, Taipei 106, Taiwan.

<sup>4</sup> National Astronomical Observatory of Japan, Osawa 2-21-1, Mitaka, Tokyo 181-8588, Japan.

<sup>5</sup> Department of Astronomy, School of Science, University of Tokyo, Bunkyo, Tokyo 113-0033, Japan.

<sup>6</sup> Nobeyama Radio Observatory, Nobeyama, Minamimaki, Minamisaku, Nagano, 384-1305, Japan.

Telescope. The ASTE Telescope, equipped with a 345 GHz receiver, is one of the most powerful facilities with which to seek molecular outflows over a wide field of views. The ASTE Telescope in the “on-the-fly” mapping mode enabled us to observe the entire region of OMC-2/3 with a high sensitivity limit (i.e., corresponding mass of the sensitivity limit is  $\sim 10^{-4} M_{\odot}$ ). The CO(3–2) emission exclusively traces higher temperature gas ( $\geq 33$  K). Our CO(3–2) results are compared with previous CO(1–0) results. We also show deep  $JHK_s$  images taken by the Simultaneous Three-Color Infrared Imager for Unbiased Survey camera (SIRIUS) on Infrared Survey Facility (IRSF), which provide us with the distributions of faint reflection nebulae, chains of knots, and jetlike features. Furthermore, we also used the archived  $24 \mu\text{m}$  data obtained by the infrared camera MIPS (Multiband Imaging Photometer) on the *Spitzer Space Telescope*, which are sensitive to hot dusty components with a temperature of  $\sim 150$  K, and probably trace 100 AU scale innermost envelopes/circumstellar disks associated with the central heating sources.

The details of the observations of the submillimeter CO(3–2) emission and the near-infrared  $JHK_s$ -bands are presented in § 2. In § 3 we show the results of the outflow survey. Data analysis of the CO(3–2) outflows is shown in § 4 and properties of the outflow driving sources are described in § 5. In § 6 we discuss the physical properties of the CO outflows in OMC-2/3 and compare them with outflows associated with low- to high-mass YSOs in previous studies. Finally, § 7 summarizes the paper.

## 2. OBSERVATIONS AND DATA REDUCTION

### 2.1. CO(3–2) Observations

The CO( $J = 3-2$ ; 345.795990 GHz) data have been taken with the ASTE 10 m telescope (Ezawa et al. 2004; Kohno et al. 2004) located at the Pampa la Bola (altitude = 4800 m), Chile. Observations were remotely made from the ASTE operation room at San Pedro de Atacama, using the network observation system N-COSMOS3 developed by NAOJ (Kamazaki et al. 2005) during the period of 2005 September 2–4. The half-power beamwidth of the ASTE Telescope is  $22''$ . We used the 345 GHz SIS heterodyne receiver, which had the typical system noise temperature of 175–350 K in DSB mode at the observed elevation. The typical atmospheric opacity at 220 GHz was 0.05 toward the zenith during our observations. The temperature scale was determined by the chopper-wheel method, which provides us with the antenna temperature corrected for the atmospheric attenuation. As a backend, we used four sets of 1024 channel autocorrelators, providing us with a frequency resolution of 31.12 KHz that corresponds to  $0.27 \text{ km s}^{-1}$  at the CO(3–2) frequency. The on-the-fly (OTF) mapping technique (Sawada et al. 2008) was employed to cover the whole OMC-2/3 region,  $23.0' \times 13.3'$  (corresponding to  $3.1 \times 1.8 \text{ pc}$  at 450 pc). The pointing of the telescope was checked every 2 hours by five-point scans of the pointlike CO(3–2) emission from O Cet (R.A. =  $02^{\text{h}}19^{\text{m}}20.8^{\text{s}}$ , decl. =  $-02^{\circ}58'40.7''$ ). The pointing errors measured during the observations range from  $1.5''$  to  $4.0''$ . To convert the antenna temperature to brightness temperature, we adopted the main-beam efficiency of 0.55, which was measured by T. Sawada et al. (2005, private communication) during the same observational semester. After subtracting linear baselines, the data were convolved by a Gaussian-tapered Bessel function (Magnum et al. 2007) whose FWHM was  $14''$  and re-sampled onto a  $7''$  grid. Since the telescope beam is a Gaussian with a FWHM of  $22''$ , the effective FWHM resolution is  $26''$  (corresponding to  $0.06 \text{ pc}$ ). The “scanning effect” was minimized by combining scans along right ascension and declination, using the PLAIT algorithm developed by Emerson & Graeve (1988).

The typical rms noise level was  $0.47 \text{ K}$  in brightness temperature ( $T_b$ ) with a velocity resolution of  $1.08 \text{ km s}^{-1}$  after smoothing over four channels.

### 2.2. Near-IR Observations

Near-IR (NIR) images in the OMC-2/3 region were obtained in 2004 November with the near-infrared camera SIRIUS (Simultaneous Three-Color Infrared Imager for Unbiased Survey) mounted on the 1.4 m Infrared Survey Facility (IRSF) Telescope at the South African Astronomical Observatory, in Sutherland. The camera is equipped with three  $1024 \times 1024$  pixel HgCdTe (HAWAII) arrays. Two dichroic mirrors enable us to make simultaneous observations at the  $J(\lambda_c = 1.25 \mu\text{m})$ ,  $H(1.63 \mu\text{m})$ , and  $K_s(2.14 \mu\text{m})$  bands. Details of the camera are provided by Nagashima et al. (1999) and Nagayama et al. (2003). The image scale of the array is  $0.45'' \text{ pixel}^{-1}$ , providing a field of view of  $7.7' \times 7.7'$  (corresponding to  $1.0 \times 1.0 \text{ pc}$ ). Three different field centers, (1) R.A. =  $5^{\text{h}}35^{\text{m}}22^{\text{s}}$ , decl. =  $-5^{\circ}00'14.8''$ , (2) R.A. =  $5^{\text{h}}35^{\text{m}}22^{\text{s}}$ , decl. =  $-5^{\circ}6'44.9''$ , and (3) R.A. =  $5^{\text{h}}35^{\text{m}}22^{\text{s}}$ , decl. =  $-5^{\circ}13'14.8''$ , were set to cover the entire OMC-2/3 region. We obtained a total exposure time of 900 s in each field. Seeing conditions were  $\sim 1.0''$  (FWHM) in the  $J$  band. The limiting magnitudes at  $J$ ,  $H$ , and  $K_s$  band were 19.2, 18.6, and 17.3 mag, respectively. We used the NOAO IRAF software package to reduce the data. We applied the standard procedures for NIR array image reduction, including dark-current subtraction, sky subtraction, and flat-fielding (see Nakajima et al. 2005 for details of the SIRIUS image processing).

## 3. RESULTS

### 3.1. Potential Star-Forming Regions in OMC-2/3

As the first step of the outflow identification described in the next section, we identified individual star-forming sites in the OMC-2/3 region. For this purpose, we compiled 1.3 mm (Chini et al. 1997; Nielbock et al. 2003) and  $350 \mu\text{m}$  (Lis et al. 1998) dust continuum sources detected in the OMC 2/3 region, finding 38 sites having dust continuum sources detected at either 1.3 mm,  $350 \mu\text{m}$ , or both. In addition, we also compiled 3.6 cm radio continuum sources observed with the VLA in the OMC 2/3 region (Reipurth et al. 1999), finding 11 radio continuum sources. Note that eight of the 11 radio continuum sources are associated with the dust continuum sources we compiled. In total, 41 sites listed in Table 1 and shown in Figure 1a are identified as potential star-forming sites located in the OMC-2/3 region.

Because some of the sites that we identified may be still in the starless or prestellar phase, we checked whether  $24 \mu\text{m}$  sources observed with *Spitzer* MIPS are associated with these potential star-forming sites. The mid-infrared  $24 \mu\text{m}$  emission, presumably tracing hot dust ( $T_{\text{dust}} \sim 150 \text{ K}$ ) around protostars, is a good indicator of ongoing star formation. Eighteen sites in Table 1 are associated with  $24 \mu\text{m}$  emission suggestive of ongoing star-forming activities.

### 3.2. Outflow Identification

The search for outflows was done based on the CO(3–2) data of the OMC-2/3 region that we obtained. The actual search, however, was limited to the vicinity of the potential star-forming sites listed in Table 1. This is because the purpose of our search is to identify outflows associated with potential star-forming sites and to compare characteristics of outflows in the following sections.

In order to identify outflows, we carefully inspected velocity channel maps of the CO(3–2) emission to see whether there is localized blueshifted or redshifted emission in the vicinity (within

TABLE 1  
CENTIMETER AND MILLIMETER/SUBMILLIMETER CONTINUUM SOURCES IN THE OMC-2/3 REGION

ID	R.A. (J2000.0)	Decl. (J2000.0)	1.3 mm <sup>a</sup>	350 $\mu$ m <sup>b</sup>	3.6 cm <sup>c</sup>	24 $\mu$ m <sup>d</sup>	Comments
1.....	05 35 30.2	−04 58 48.0	SIMBA <i>a</i>	CSO 1	...	053530-045848	
2.....	05 35 29.7	−04 58 06.0	SIMBA <i>b</i>	...	...	...	
3.....	05 35 28.2	−04 58 40.0	SIMBA <i>c</i>	...	...	053528-045838	
4.....	05 35 28.6	−04 57 48.0	SIMBA <i>d</i>	...	...	...	
5.....	05 35 30.6	−04 59 49.0	SIMBA <i>e</i>	...	...	...	
6.....	05 35 35.1	−04 59 24.5	...	CSO 2	...	...	
7.....	05 35 15.8	−04 59 58.7	...	CSO 3	...	053516-050003 and 053515-050009	Binary
8.....	05 35 17.1	−05 00 02.8	...	CSO 4	...	...	
9.....	05 35 18.0	−05 00 19.8	MMS 1	CSO 5	...	...	
10.....	05 35 18.3	−05 00 34.8	MMS 2	CSO 6	VLA 1	053518-050034	Binary (from Nielbock et al. 2003)
11.....	05 35 19.2	−05 00 51.2	MMS 3	CSO 7	...	053519-050051	
12.....	05 35 20.5	−05 00 53.0	MMS 4	CSO 8	...	...	
13.....	05 35 22.4	−05 01 14.1	MMS 5	CSO 9	...	053522-050115	
14.....	05 35 23.5	−05 01 32.2	MMS 6	CSO 10	VLA 3	053524-050130 and 053524-050140	Multiple systems?
15.....	05 35 27.2	−05 03 38.5	...	CSO 11	...	...	
16.....	05 35 26.4	−05 03 53.4	MMS 7	CSO 12	VLA 4	053527-050355	Bright reflection nebula, Haro- 5a/6a (from Haro 1953)
17.....	05 35 26.5	−05 05 17.4	MMS 8	CSO 13	...	...	
18.....	05 35 26.0	−05 05 42.4	MMS 9	CSO 14	VLA 5	053526-050546	Extended 24 $\mu$ m source
19.....	05 35 32.3	−05 05 41.8	MMS 10	...	...	...	
20.....	05 35 25.6	−05 07 57.4	...	...	VLA 9	053526-050758	Located at the edge of the OMC-2 dust filament
21.....	05 35 22.9	−05 06 41.2	...	CSO 15	...	...	
22.....	05 35 23.7	−05 07 10.2	FIR 1 <i>c</i>	CSO 16	VLA 7	...	Extended 24 $\mu$ m and cm source
23.....	05 35 23.4	−05 07 32.2	FIR 1 <i>b</i>	CSO 17	...	...	
24.....	05 35 24.6	−05 07 53.3	FIR 1 <i>a</i>	CSO 18	VLA 8	053524-050753	Faint 24 $\mu$ m source
25.....	05 35 24.7	−05 12 33.3	...	CSO 19	...	...	
26.....	05 35 24.3	−05 08 33.3	FIR 2	CSO 20	...	053524-050831	
27.....	05 35 26.5	−05 08 25.4	...	CSO 21	...	...	
28.....	05 35 27.5	−05 09 32.5	FIR 3	CSO 22	VLA 11	053528-050935	A 24 $\mu$ m source (SP 053527-050923) is located
29.....	05 35 26.7	−05 10 00.4	FIR 4	CSO 23	VLA 12	053527-051002	At $\sim 10''$ northwest from FIR 3
30.....	05 35 24.8	−05 10 29.5	...	...	VLA 13	053525-051031	mm/sub-mm and 24 $\mu$ m sources do not coincide with the cm source
31.....	05 35 26.4	−05 10 23.4	FIR 5	CSO 24	...	...	Bright conelike NIR feature
32.....	05 35 26.3	−05 12 23.4	...	CSO 26	...	...	
33.....	05 35 24.7	−05 12 33.3	...	CSO 27	...	...	
34.....	05 35 23.4	−05 12 36.2	FIR 6 <i>a</i>	CSO 28	...	...	
35.....	05 35 21.7	−05 12 13.1	...	...	VLA 14	...	
36.....	05 35 23.4	−05 12 03.2	FIR 6 <i>b</i>	CSO 25	...	053523-051205	
37.....	05 35 21.5	−05 13 15.1	FIR 6 <i>c</i>	CSO 29	...	...	
38.....	05 35 20.0	−05 13 14.9	FIR 6 <i>d</i>	CSO 30	...	053520-051314	
39.....	05 35 21.5	−05 14 30.1	No obs.	CSO 31	...	...	
40.....	05 35 21.3	−05 14 54.0	No obs.	CSO 32	...	...	
41.....	05 35 19.5	−05 15 34.9	No obs.	CSO 33	...	053520-051533	Extended 24 $\mu$ m source?

NOTE.—Units of right ascension are hours, minutes, and seconds, and units of declination are degrees, arcminutes, and arcseconds.

<sup>a</sup> 1.3 mm continuum source names are from Chini et al. (1997) and Nielbock et al. (2003).

<sup>b</sup> 350  $\mu$ m continuum source names are from Lis et al. (1998).

<sup>c</sup> 3.6 cm continuum source names are from Reipurth et al. (1999).

<sup>d</sup> We identified 24  $\mu$ m sources obtained from the archive data taken by *Spitzer*/MIPS using the IRAF *apphot* package.

a radius of  $\sim 1'$  of each site in Table 1. We also used our *JHK<sub>s</sub>* images to see whether there were any reflection nebulae, jetlike features, or a chains of knots, which are suggestive of the existence of outflows, in the vicinity of each site in Table 1.

With these search procedures, we identified 21 outflow candidates, which were then classified into three categories, “clear,” “possible,” and “marginal” as follows:

1. *Clear*.—Outflows in this category have both localized blue- and redshifted lobes with clear bipolarity in the CO(3–2) channel maps.

2. *Probable*.—Outflows in this category have either a localized blue- or redshifted lobe in the CO(3–2) channel maps.

3. *Marginal*.—Outflows in this category have neither localized blue- or redshifted lobes in the CO(3–2) channel maps, but are associated with extended CO(3–2) high-velocity emission and/or NIR features suggestive of an outflow in the *JHK<sub>s</sub>* images.

With this classification, 10 outflow candidates were classified as clear, four were classified as probable, and six were classified as marginal. Table 2 shows the summary of the outflow search for each of the potential star-forming sites. Figures 1*b* and 1*c*



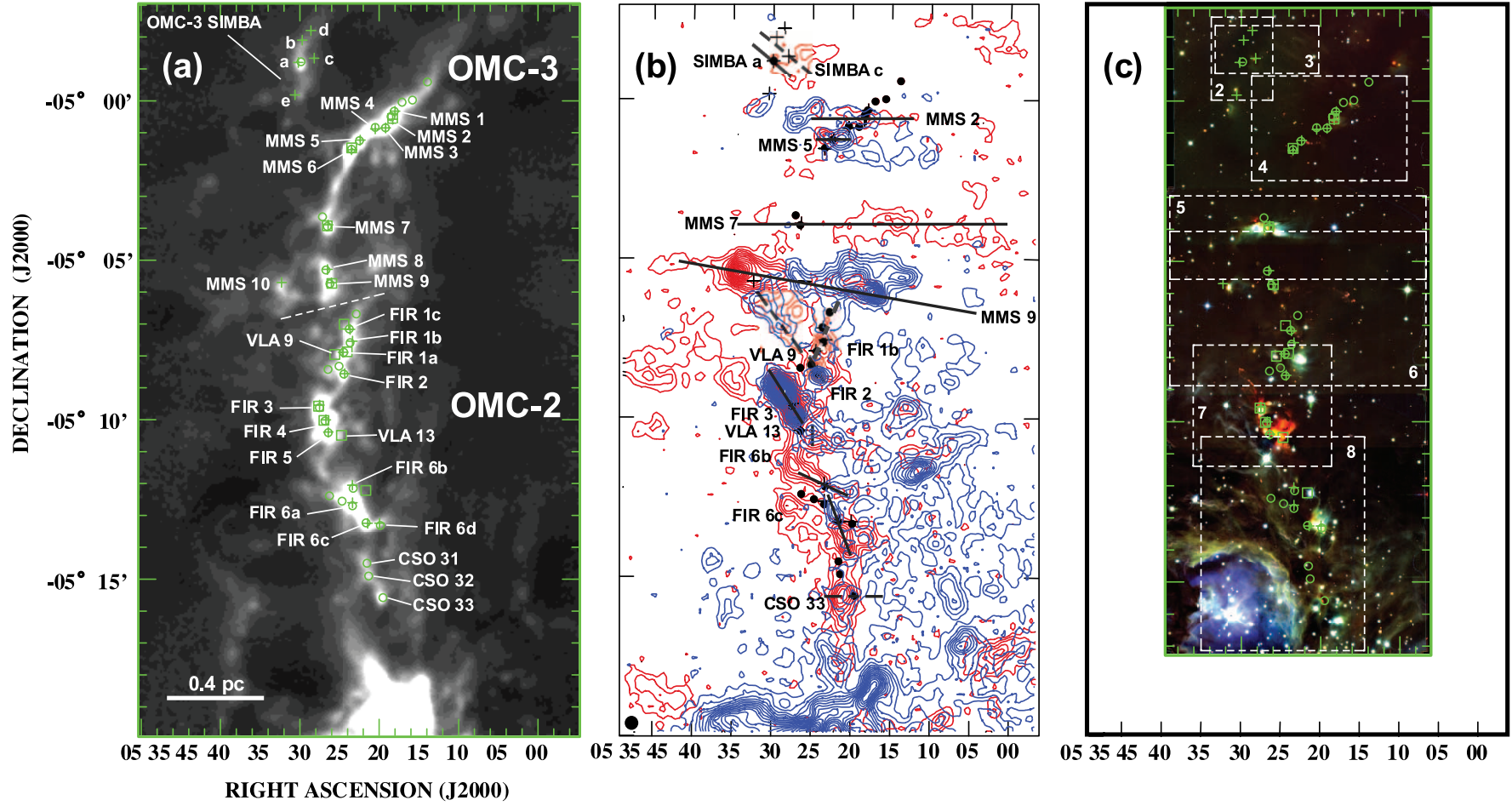


FIG. 1.—(a) 850  $\mu\text{m}$  dust continuum map of the OMC-2/3 region from Johnstone & Bally (1999). (b) Averaged intensity map of the CO(3–2) emission taken with the ASTE with a velocity range of blue and red contours are  $V_{\text{LSR}} = -6.2\text{--}7.8 \text{ km s}^{-1}$  and  $V_{\text{LSR}} = 14.3\text{--}27.3 \text{ km s}^{-1}$ , respectively. Contour intervals are  $0.45 \text{ K km s}^{-1}$  starting at  $0.45 \text{ K km s}^{-1}$ . Solid and dashed lines show outflow axes categorized as clear (SIMBA *a*, MMS 2, MMS 5, MMS 7, MMS 9, FIR 2, FIR 3, VLA 13, FIR 6*b*, and FIR 6*c*) and probable (SIMBA *c*, VLA 9, FIR 1*b*, and CSO 33), respectively. (c) The composite image taken by the IRSF/SIRIUS. Pseudo colors of blue, green, and red show the data of  $J$ -,  $H$ -, and  $K_s$  bands, respectively. Dashed squares in panel *c* show the focusing areas in Figs. 2–6 and Figs. 8 and 9. Numbers in the squares correspond to the figure numbers. Crosses, dots, and squares indicate positions of 1.3 mm, 350  $\mu\text{m}$ , and 3.6 cm sources, respectively (from Chini et al. 1997; Lis et al. 1998; Nielbock et al. 2003).

TABLE 2  
IDENTIFICATION OF THE CO(3–2) OUTFLOWS

ID	Object Name <sup>a</sup>	Identification <sup>b</sup>	Map <sup>c</sup>	NIR Features <sup>d</sup>	Reference	Comments
1.....	SIMBA <i>a</i>	C	BR		1	
3.....	SIMBA <i>c</i>	P	BR?	[1]	1	Faint reflection nebula are associated with blueshifted CO emission, monopolar flow?
6.....	CSO 2	M	BR		1, 2	No Gaussian line profile, may trace a part of motion of large scale cloud gas
10.....	MMS 2	C	BR	[2], [3], [4]	1, 2, 3	Corresponding to “flow B,” <sup>e</sup> nearly plane of the sky
13.....	MMS 5	C	BR	[5]	1, 2, 3	Corresponding to “flow C,” <sup>e</sup> H <sub>2</sub> chain of knots
14.....	MMS 6	M	BR	[6]	1	Faint jetlike feature in the NIR image associated with SP 053524-050130
16.....	MMS 7	C	BR	[7]	1, 2, 3, 4	Corresponding to “flow F,” <sup>e</sup> nearly plane of the sky
18.....	MMS 9	C	BR	[9], [10], [11]	1, 2, 3	Corresponding to “flow H,” <sup>e</sup>
20.....	VLA 9	P	B	[13]	1	Monopolar flow, edge of the dust filament
23.....	FIR 1 <i>b</i>	P	BR		1, 2, 3	
26.....	FIR 2	C	BR		1, 3	
28.....	FIR 3	C	BR	[14]	1, 2, 5	“Butterfly-like” velocity structure
<sup>f</sup> .....	MIR 20	M	B	[15]	1	There is a 24 $\mu$ m source, SP 053527-050923 and Bright NIR jet
29.....	FIR 4	M	BR?	[16]	1	Faint reflection nebula?
30.....	VLA 13	C	BR	[17]	1	Bright NIR feature
36.....	FIR 6 <i>b</i>	C	BR		1	
37.....	FIR 6 <i>c</i>	C	BR		1	
40.....	CSO 32	M	BR		1	Another possibility might be due to gas associated with shocked gas produced by HII region
41.....	CSO 33	P	BR	[19]	1	Another possibility might be due to gas associated with shocked gas produced by HII region

<sup>a</sup> Object names from Chini et al. (1997), Nielbock et al. (2003), Lis et al. (1998), and Reipurth et al. (1999).

<sup>b</sup> Outflow identification results based on the CO(3–2) emission and *JHK<sub>s</sub>* image. C, P, and M indicate outflows identified as clear, probable, and marginal, respectively.

<sup>c</sup> Bipolarity of the CO(3–2) emission based on channel maps. B and R denote the blueshifted and redshifted CO(3–2) emission, respectively.

<sup>d</sup> Notation of near-infrared features (see Fig. 2–6 and Figs. 8 and 9).

<sup>e</sup> Flows were identified in the 2.12  $\mu$ m  $v = 1-0$  s(1) H<sub>2</sub> line emission (Yu et al. 1997).

<sup>f</sup> CO(3–2) emission and NIR jetlike feature were detected at this source.

REFERENCES.—(1) This work; (2) Aso et al. 2000; (3) Williams et al. 2003; (4) Takahashi et al. (2006); Wu et al. 2005.

show an overall distribution of the 14 outflows candidates categorized as either clear or probable. Among these 14 outflow candidates, seven were also previously found in CO(1–0) (Aso et al. 2000; Williams et al. 2003). The other seven outflow candidates were newly identified in our observations. We also detected *Spitzer* 24  $\mu$ m sources toward 12 out of the 14 outflows as the likely outflow-driving candidate. Eight sources having near-infrared features suggestive of outflows were identified. In the next section, we describe the results of individual outflow candidates in detail.

### 3.3. Individual Outflows

In this section we present individual outflows identified in this paper. We also present possible outflow candidates which are not associated with any of the 41 potential star-forming sites in § 3.4. In the outflow identification, we adopt the source name based on the 1.3 mm sources by Chini et al. (1997) and Nielbock et al. (2003). If driving sources have no 1.3 mm sources, we adopt the 350  $\mu$ m and/or VLA 3.6 cm source name, which were identified by Lis et al. (1998) and Reipurth et al. (1999), respectively.

#### 3.3.1. OMC-3 SIMBA Region

Five of the 41 potential star-forming sites are located in the northeastern OMC-3 region, called the “SIMBA” region (Nielbock et al. 2003). In this region, we newly identified two outflow candidates in CO(3–2); one, categorized as clear, is associated with SIMBA *a* as shown in Figure 2, and the other, categorized as probable, is associated with SIMBA *c* as shown in Figure 3. The later one associated with SIMBA *c* has only a blueshifted lobe, in which a faint NIR nebula denoted by [1] in Figure 3*a* is found. Note that both the blueshifted lobe and the NIR nebula show

elongation in the same direction (northeast-southwest). The elongated CO and NIR structures would support the presence of the outflow associated with SIMBA *c*. Although there is redshifted CO(3–2) emission to the west of SIMBA *c*, which could be a counterpart of the blueshifted lobe, it is difficult to conclude that this redshifted emission is a part of the outflow associated with SIMBA *c*, because the orientation of the redshifted emission (east–west) is very different from that of the blueshifted lobe, and also because the redshifted emission is not clearly isolated from the ambient cloud. Both SIMBA *a* and SIMBA *c* are associated with *Spitzer* 24  $\mu$ m sources (SP 053530-045848 and 053528-045838, respectively) as shown in Figure 2*b*, and they could be the driving sources of these outflows.

#### 3.3.2. OMC-3 Region

Figures 4–6 show results of our outflow survey in the OMC-3 region (except the SIMBA region). Fourteen of 41 potential star-forming sites are located in this region, and at least six 1.3 mm sources have a class 0-type SEDs with a small ratio of  $L_{\text{bol}}/L_{\text{mm}} < 200$  (Chini et al. 1997). We identified four CO(3–2) outflows categorized as clear in this region.

*MMS 2 (clear).*—We detected a CO(3–2) outflow along the east-west direction toward MMS 2 as shown in Figure 4*b*. The blue- and redshifted components overlap, suggesting that the axis of this flow is close to the plane of the sky. This east-west outflow has also been identified in the CO(1–0) emission (Williams et al. 2003, Aso et al. 2000). However, the previous CO(1–0) studies had difficulty identifying which sites of MMS 1–4 the CO outflow is associated with. Because only MMS 2 is associated with a significant 24  $\mu$ m *Spitzer* source (SP 053518-050045), this CO(3–2) outflow, presumably driven by the 24  $\mu$ m *Spitzer* source, is most

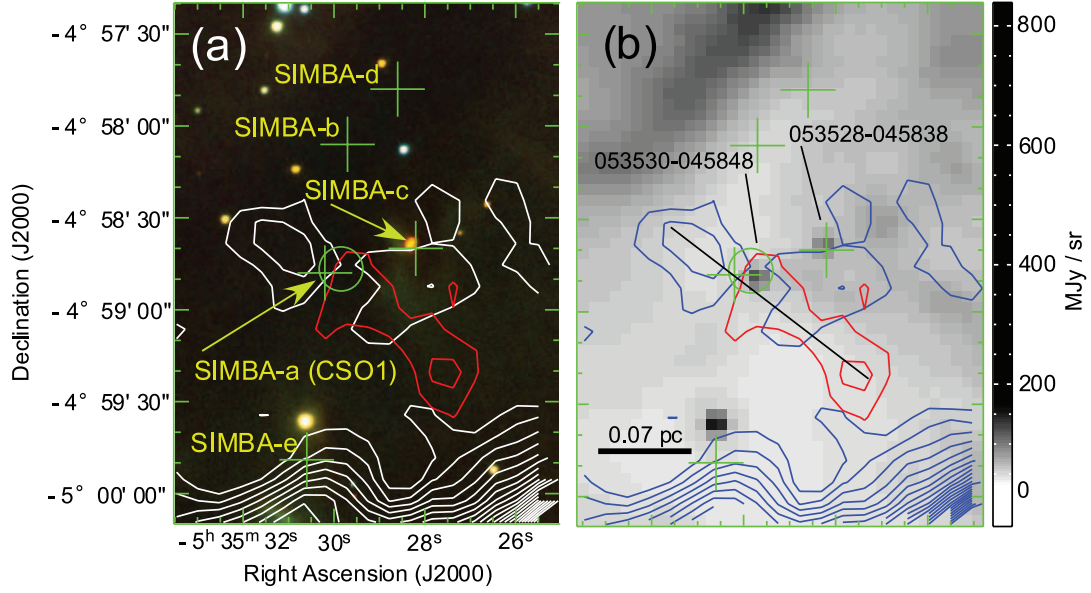


FIG. 2.—Images of SIMBA: (a)  $JHK_s$  image taken by the IRSF/SIRIUS (color) superposed on the CO(3–2) emission taken with the ASTE Telescope (contours). (b) 24  $\mu\text{m}$  image taken with the *Spitzer* MIPS (gray scale) superposed on the CO(3–2) emission taken with the ASTE Telescope (contours). The blue (white in panel a) and red contours show the blue- and redshifted components in the velocity range of  $7.8 \text{ km s}^{-1} \leq V_{\text{LSR}} \leq 8.9 \text{ km s}^{-1}$  and  $15.4 \text{ km s}^{-1} \leq V_{\text{LSR}} \leq 16.5 \text{ km s}^{-1}$ , respectively. Contour intervals are  $1.13 \text{ K km s}^{-1}$  starting at  $2.25 \text{ K km s}^{-1}$ . Solid lines in panel b indicate an outflow axis categorized as clear in panel a. Crosses and open circles indicate positions of 1.3 mm and 350  $\mu\text{m}$  sources, respectively (from Nielbock et al. 2003; Lis et al. 1998).

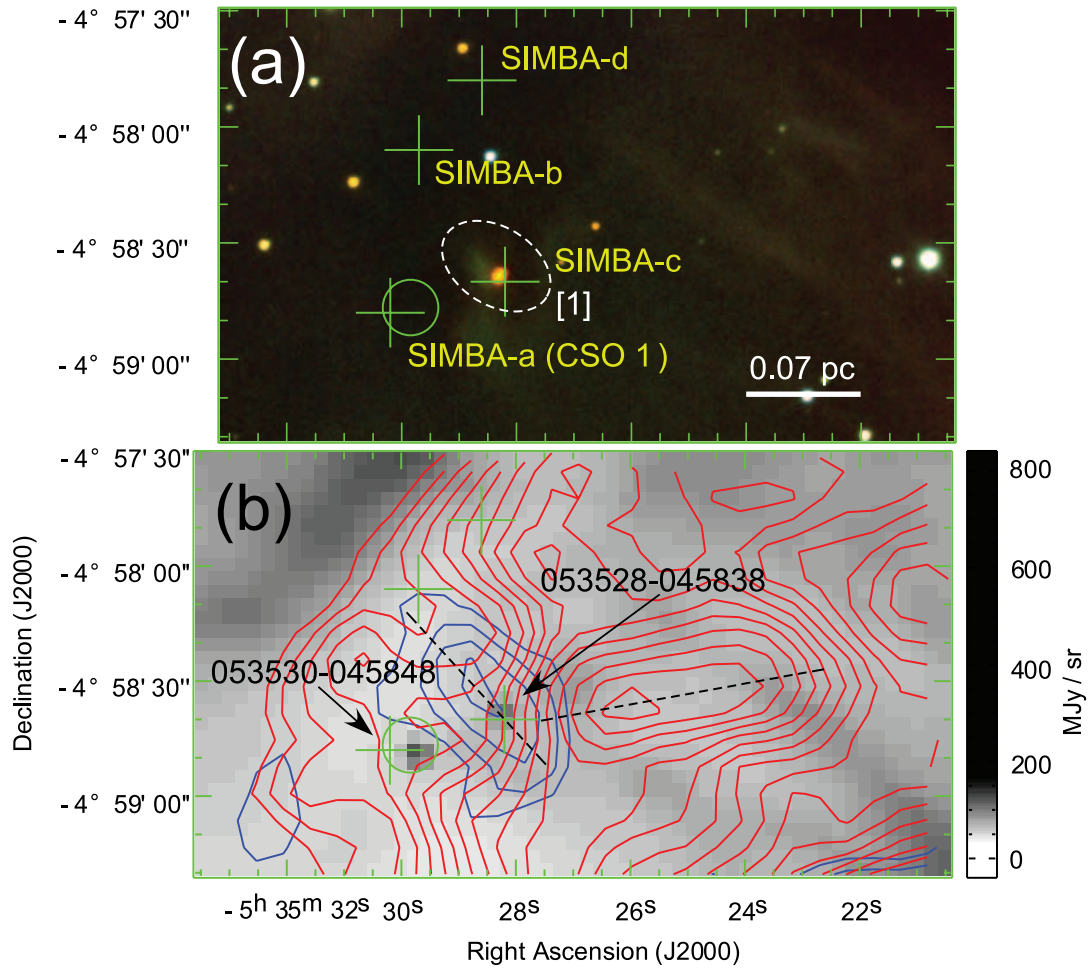


FIG. 3.—Images of SIMBA: (a)  $JHK_s$  image taken by the IRSF/SIRIUS. (b) 24  $\mu\text{m}$  image taken with the *Spitzer* MIPS (gray scale) superposed on the CO(3–2) emission taken with the ASTE Telescope (contours). The blue and red contours in panel b show the blue- and redshifted components in the velocity range of  $8.9 \text{ km s}^{-1} \leq V_{\text{LSR}} \leq 10.1 \text{ km s}^{-1}$  and  $13.5 \text{ km s}^{-1} \leq V_{\text{LSR}} \leq 14.2 \text{ km s}^{-1}$ , respectively. Contour intervals are  $1.50 \text{ K km s}^{-1}$  starting at  $10.0 \text{ K km s}^{-1}$ . A dashed line in panel b indicates direction of the outflow categorized as probable. Crosses and open circles indicate positions of 1.3 mm and 350  $\mu\text{m}$  sources, respectively (from Nielbock et al. 2003; Lis et al. 1998). Dashed ellipses shows the position of NIR features presented in Table 2.



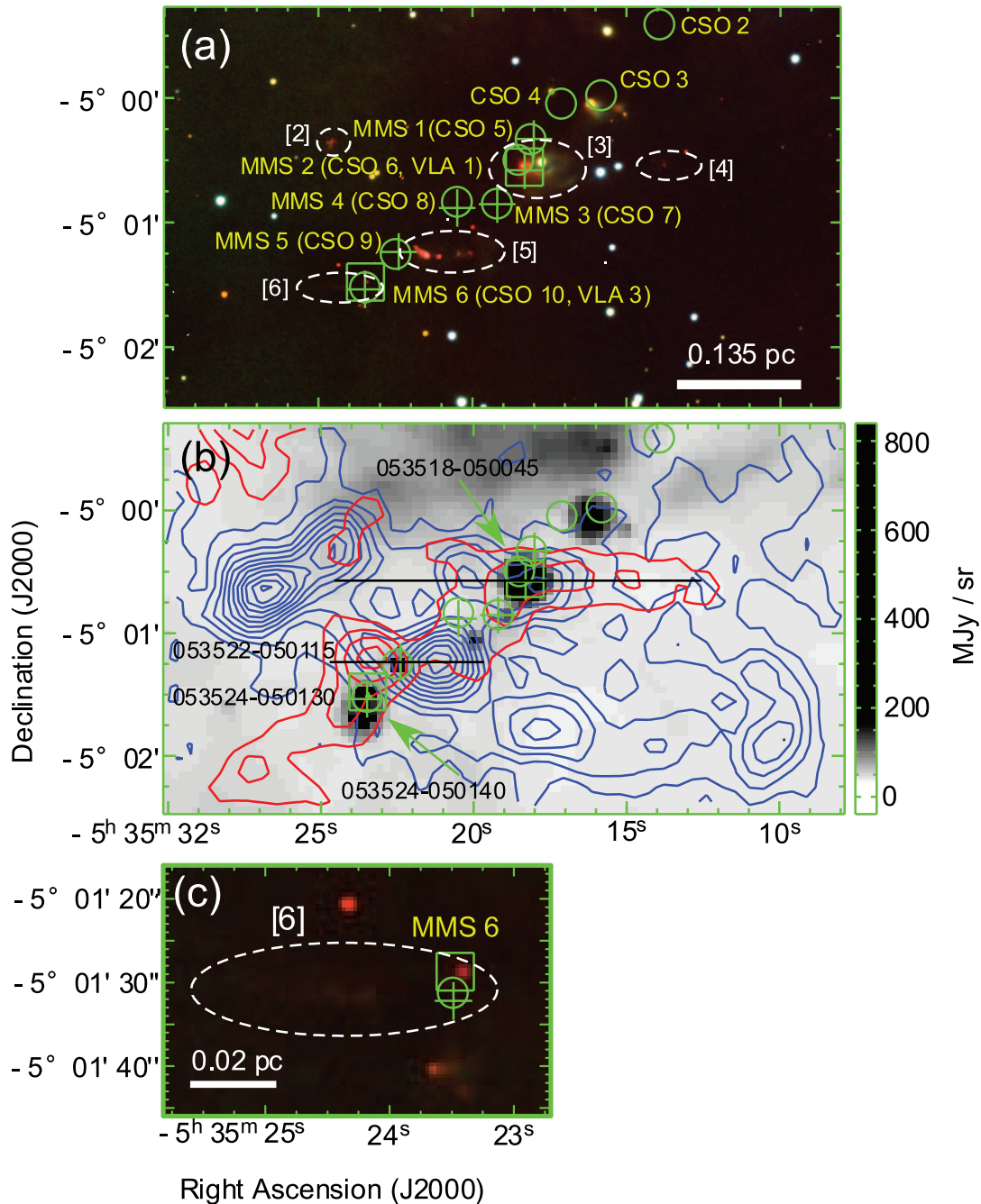


FIG. 4.—Images in the northern part of the OMC-3 region. (a)  $JHK_s$  image taken by the IRSF/SIRIUS. (b)  $24\ \mu\text{m}$  image taken with the *Spitzer* MIPS (gray scale) superposed on the CO(3–2) high-velocity emission taken with the ASTE Telescope (contours). The blue and red contours show the blue- and redshifted components in the velocity range of  $1.3\ \text{km s}^{-1} \leq V_{\text{LSR}} \leq 6.7\ \text{km s}^{-1}$  and  $14.3\ \text{km s}^{-1} \leq V_{\text{LSR}} \leq 15.4\ \text{km s}^{-1}$ , respectively. Contour intervals are  $2.4\ \text{K km s}^{-1}$  starting at  $3.6$  and  $1.46\ \text{K km s}^{-1}$  starting at  $2.19\ \text{K km s}^{-1}$ , respectively. (c) Zoom up view of the  $JHK_s$  image toward MMS 6. A solid line in panel b indicates the outflows categorized as clear associated with MMS 2 and MMS 5. Crosses, open circles, and open squares indicate positions of  $1.3\ \text{mm}$ ,  $350\ \mu\text{m}$  and  $3.6\ \text{cm}$  sources, respectively (from Chini et al. 1997; Lis et al. 1998; Reipurth et al. 1999). Dashed ellipses show the positions of NIR features presented in Table 2.

probably associated with MMS 2 rather than MMS 1, MMS 3 or MMS 4. In the NIR image shown in Figure 4a, there is a jetlike feature and a knot to the west of the *Spitzer* source (denoted by [3] and [4], respectively). These two features were also detected in NIR H<sub>2</sub> emission (Yu et al. 1997; Stanke et al. 2002; Tsujimoto et al. 2004). Both of them are elongated in the same direction and in particular the reflection nebula denoted by [3] is spatially coincident with the blueshifted lobe. An extended NIR feature was also detected in the eastern part of the MMS 2 along the outflow axis (denoted by [2]). Our  $JHK_s$  image suggests that the NIR

feature is a reflection nebula from the isolated star-forming site rather than knots from MMS 2 (§ 3.4), although previous NIR H<sub>2</sub> observations suggested that the origin of the NIR feature is the outflow from MMS 2.

**MMS 5 (clear).**—There is a compact east-west outflow with a clear bipolarity centered on MMS 5, as shown in Figure 4b. This east-west outflow has also been identified in the CO(1–0) emission (Williams et al. 2003; Aso et al. 2000). A  $24\ \mu\text{m}$  source (SP 053522-050115), associated with MMS 5, is located between the blue- and redshifted lobes, suggesting that this  $24\ \mu\text{m}$  source

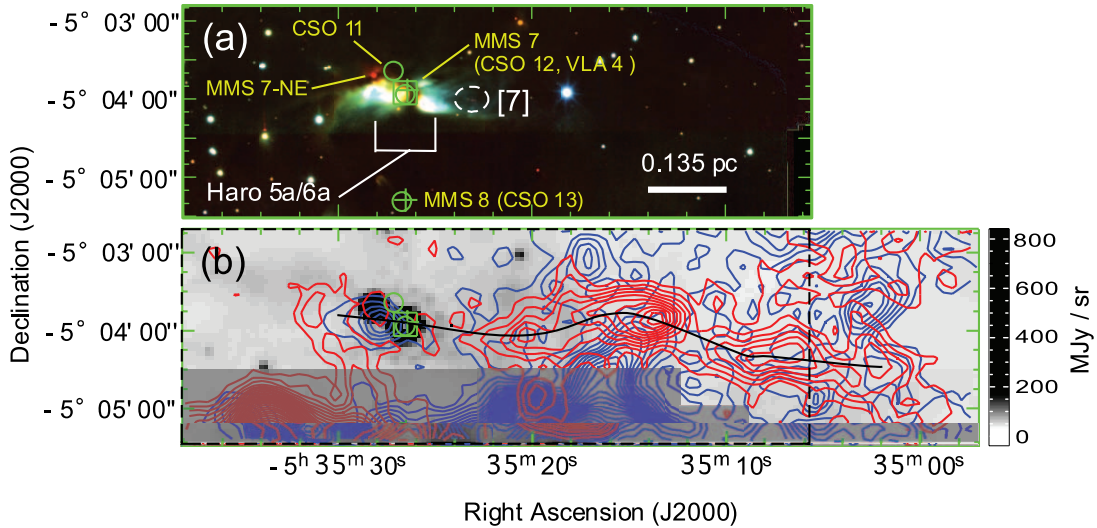


FIG. 5.—Images of MMS 7. (a)  $JHK_s$  image taken by the IRSF/SIRIUS. (b)  $24\ \mu\text{m}$  image taken with the *Spitzer* MIPS (gray scale) superposed on the CO(3–2) emission taken with the ASTE Telescope (contours). The blue and red contours in panel b show the blue- and redshifted components in the velocity range of  $6.7\ \text{km s}^{-1} \leq V_{\text{LSR}} \leq 7.8\ \text{km s}^{-1}$  and  $14.3\ \text{km s}^{-1} \leq V_{\text{LSR}} \leq 16.5\ \text{km s}^{-1}$ , respectively. Contour intervals are  $1.26\ \text{K km s}^{-1}$  starting at  $1.89\ \text{K km s}^{-1}$  and  $1.74\ \text{K km s}^{-1}$  starting at  $2.61\ \text{K km s}^{-1}$ , respectively. A solid line in panel b traces the local peaks of the CO outflow associated with MMS 7 which are categorized as clear. Crosses, open circles, and open squares indicate positions of 1.3 mm,  $350\ \mu\text{m}$  and 3.6 cm sources, respectively (from Chini et al. 1997; Lis et al. 1998; Reipurth et al. 1999). Dashed ellipses show the position of NIR features presented in Table 2. The gray area in the bottom part of panel b shows the bipolar outflow from the source, MMS 9, located south of MMS 7.

is most probably the driving source of the outflow. The infrared image in Figure 4a shows that several knots, denoted by [5], are associated with the blueshifted lobe. These knots were also detected in infrared  $\text{H}_2$  emission (Yu et al. 1997; Stanke et al. 2002).

**MMS 6 (marginal).**—MMS 6 is the brightest 1.3 mm continuum source in the OMC-2/3 region (Chini et al. 1997). We did not find any clear signature of CO(3–2) outflows (see Fig. 4b), as also indicated by previous CO(1–0) observations (Williams et al. 2003; Matthews et al. 2005), although there is extended high-velocity redshifted emission to the southeast of MMS 6. Careful inspection of the near-infrared image in Figure 4c, however, shows that there are two faint  $K_s$  emissions north and south of MMS 6. These two northern and southern sources are also detected at  $24\ \mu\text{m}$  (SP 053524-050130 and SP 053524-050140, respectively). More importantly, the near-infrared image shows a faint jetlike feature denoted by [6] to the east of the northern infrared source. In addition, a 3.6 cm free-free emission (i.e., VLA 3) is also associated with the northern infrared source. These results suggest that there may be an east-west outflow associated with the northern infrared source. We note that previous studies (Yu et al. 1997, Stanke et al. 2002) considered the two infrared sources north and south of MMS 6 to be knots due to a jet, although we consider them to be protostars because they are more pointlike and are detected even at  $24\ \mu\text{m}$ .

**MMS 7 (clear).**—Figure 5 shows a molecular outflow associated with MMS 7, which is elongated in the east-west direction. While the outflow shows a clear bipolarity, the redshifted lobe is much more elongated than the blueshifted lobe. The connected trajectory of the CO redshifted emission peaks, denoted as a black solid curve in Figure 5b, shows a wiggled structure over 1 parsec to the west of MMS 7, possibly suggesting a precessing motion. This east-west outflow has also been identified in the CO(1–0) observations by Aso et al. (2000), Williams et al. (2003), and Takahashi et al. (2006). The projected maximum velocity of this outflow is relatively small, and the NIR reflection nebula (Haro-5a/6a; Haro 1953) associated with the outflow extends to both east and west. These suggest that the outflow is almost on the plane of the sky. In addition, there is a one-sided optical jet

on the western side (Reipurth et al. 1997; HH 294) and a compact 3.6 cm free-free jet associated with the central star (Reipurth et al. 1999, 2004), both of which have roughly the same position angle as that of the CO(3–2) flow. We also detected faint knots along the western part of the CO outflow as denoted by [7] in Figure 5a. We note that the CO outflow associated with MMS 7 has a very large collimation factor, 15.4, for blueshifted component, which is significantly larger than the others, 0.9–4.7.<sup>7</sup> We do not understand how to make such a large collimation factor of CO outflows, but this kind of CO outflow might be related to optical jets on a parsec scale (Reipurth et al. 1997).

In the northeast of the MMS 7, there is an embedded protostellar candidate, MMS 7-NE, which has been identified by Takahashi et al. (2006), although the source is not included in the 41 potential star-forming sites. A possible compact bipolar outflow associated with MMS 7-NE was detected in the interferometric CO(1–0) observations with a 0.05 pc scale (Takahashi et al. 2006). The CO(3–2) bipolar outflow associated with the MMS 7-NE was not detected probably due to the insufficient spatial resolution and potential contamination of the MMS 7 outflow emission.

**MMS 9 (clear).**—A prominent CO(3–2) outflow elongated from east to west was detected as shown in Figure 6b. This outflow has also been identified by CO(1–0) observations (Aso et al. 2000; Williams et al. 2003). The outflow shows clear bipolarity centered on MMS 9. The blue- and redshifted lobes are east and west of MMS 9. An additional redshifted lobe was also detected overlapping part of the blueshifted lobe. The maximum size of the outflow was measured at up to one pc in channel maps. A  $24\ \mu\text{m}$  emission (SP 053526-050546) is associated with MMS 9, and is presumably the driving source of the outflow, although there is another  $24\ \mu\text{m}$  source (SP 053526-050558) located at  $10''$  south of MMS 9. In the  $JHK_s$  image (see Fig. 6a), we detected a near-infrared feature denoted by [9] located to the east of the  $24\ \mu\text{m}$

<sup>7</sup> The axis ratio ( $R_{\text{maj}}/R_{\text{min}}$ ) was adopted the maximum size of major- and minor- axes measured by eyes.



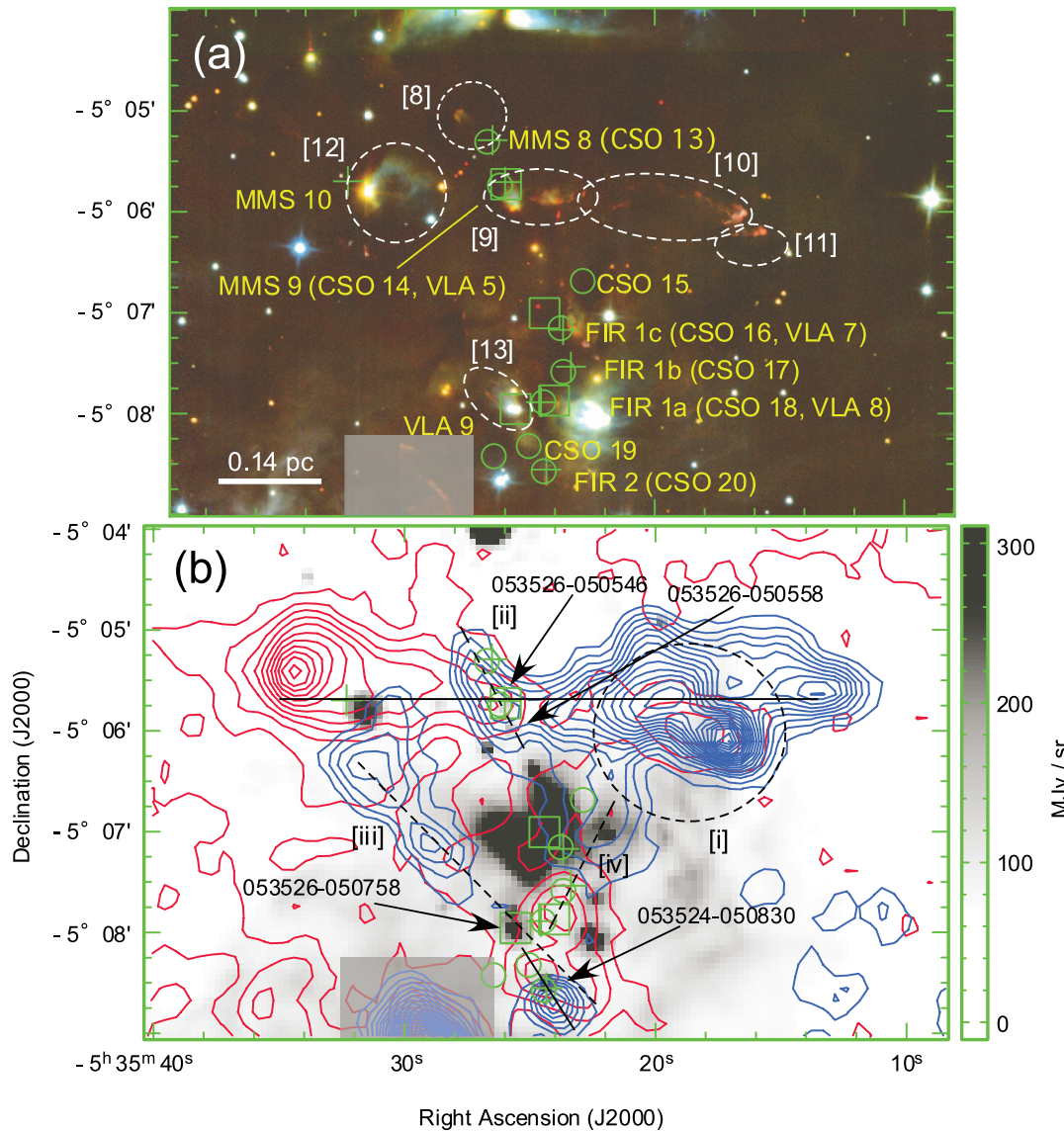


FIG. 6.—Images in the MMS 8 to FIR 1 region. (a)  $JHK_s$  image taken by the IRSF/SIRIUS. (b)  $24\ \mu\text{m}$  image taken with the *Spitzer* MIPS (gray scale) superposed on the CO(3-2) emission taken with the ASTE Telescope (contours). The blue and red contours show the blue- and redshifted components in the velocity range of  $-1.9\ \text{km s}^{-1} \leq V_{\text{LSR}} \leq 6.7\ \text{km s}^{-1}$  and  $14.3\ \text{km s}^{-1} \leq V_{\text{LSR}} \leq 21.9\ \text{km s}^{-1}$ , respectively. Contour intervals are  $6.90\ \text{K km s}^{-1}$  starting at  $4.14\ \text{K km s}^{-1}$  and  $4.62\ \text{K km s}^{-1}$  starting at  $7.70\ \text{K km s}^{-1}$ , respectively. Solid, dashed, and dash-dotted lines in panel b show the outflows categorized as clear (east-west outflow associated with MMS 9), probable (associated with VLA 9 and FIR 1b), marginal (northeast-southwest outflow associated with MMS 9), respectively. Crosses, open circles, and open squares indicate positions of  $1.3\ \text{mm}$ ,  $350\ \mu\text{m}$  and  $3.6\ \text{cm}$  sources, respectively (from Chini et al. 1997; Lis et al. 1998; Reipurth et al. 1999). Hatched areas are outflow contamination from southern part, FIR 3 (see Fig. 8). Dashed ellipses show the positions of NIR feature presented in Table 2.

source (SP 053526-050546). In addition, there appear bow-shock-like features as denoted by [10] and [11] in Figure 6a, which seem to be associated with the termination of the blueshifted (or redshifted) CO knots presented in Figure 6b, denoted by [i]. It is interesting to note that the velocity width of the blueshifted emission abruptly increases at the position of the bow-shock-like features as shown in the position-velocity diagram (see Fig. 7).

Figure 6b shows that there are two other outflow candidates in this region. One is the blueshifted lobe elongated to the northeast denoted by [ii] from the position of the  $24\ \mu\text{m}$  sources (SP 053526-050546 and SP 053526-050558). At the northeast end of the blueshifted lobe, there is a faint bow-shock-like feature detected in the  $JHK_s$  image shown in Figure 6a (denoted by [8]). It is not clear whether this blueshifted lobe is a part of the outflow described above, or another outflow having no clear redshifted lobe. In the following discussion, we consider that this blueshifted

lobe is a part of the outflow associated with MMS 9. The other outflow candidate is the extended reflection nebula, located at  $\sim 15''$  west of MMS 10 (denoted as [12] in Figure 6a). There is an infrared point source identified as J05353153-0505473 in the 2MASS catalog to the east of the reflection nebula. Even though the source sits inside the redshifted outflow from MMS 9, it is probably not related to the high-velocity emission. This is because the source already appears in the  $J$ -band as a point source, suggesting that it is more evolved than other potential star-forming sites.

### 3.3.3. OMC-2 Region

The OMC-2 region contains embedded clusters with approximately 100 stellar components (Lada & Lada 2003). There are also mid-infrared sources with a number density of  $200\ \text{pc}^{-2}$  in the most complex regions: FIR 3–FIR 5 (Nielbock et al. 2003). Several bright reflection nebulae and NIR features in this region

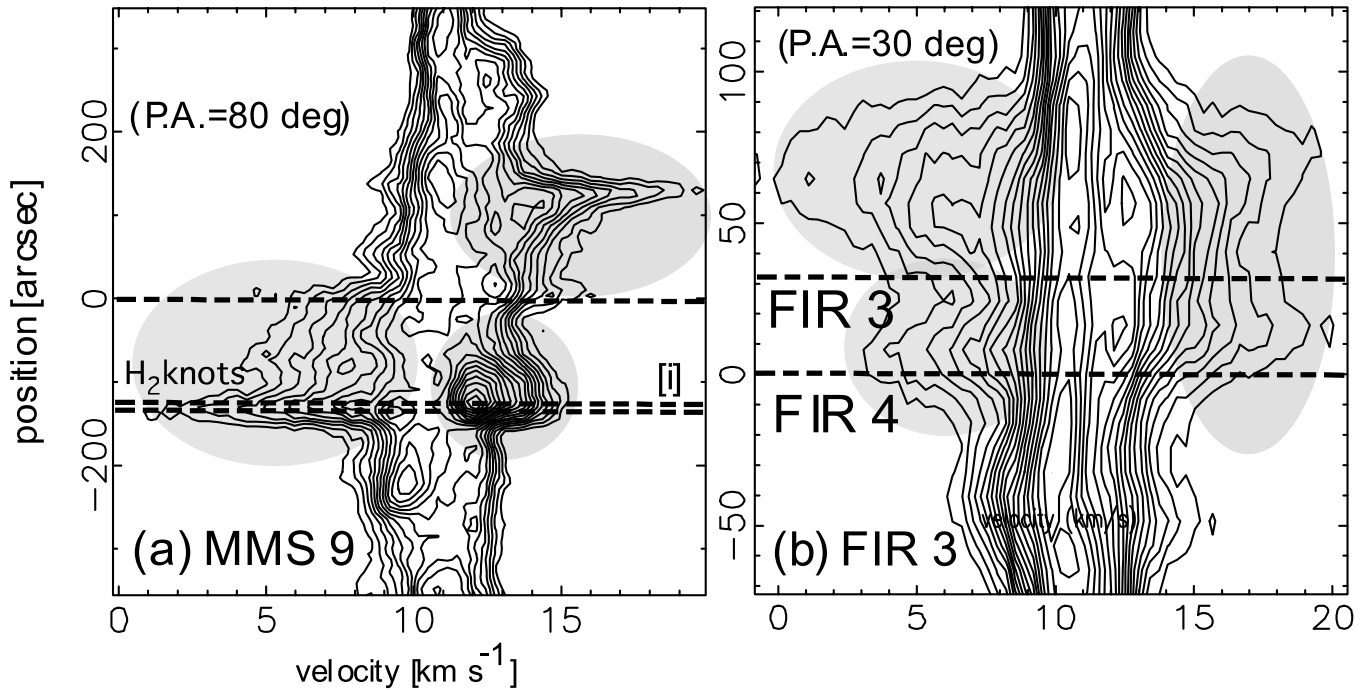


FIG. 7.—Position-velocity diagrams in the CO(3–2) emission along the major axis toward detected outflows in OMC-2/3. The contour starting level and increment are 10% and 5% level of the peak intensity, respectively. The reference position of each figure set on the positions of 1.3 mm peak.

indicate an extreme complexity. Twenty-one of the 41 potential star-forming sites are included in this region.

**VLA 9 (probable).**—A blueshifted outflow is detected to the northeast of VLA 9, which is associated with a 24  $\mu$ m source, SP 053526-050758, as shown by the dotted-line [iii] in Figure 6b. We consider that this blueshifted outflow is probably driven by the 24  $\mu$ m source associated with VLA 9, although previous studies have reported that the blueshifted outflow is associated with MMS 10 (Williams et al. 2003; Aso et al. 2000). This is because (1) MMS 10 is more likely a starless core rather than a protostellar core since there is no 24  $\mu$ m source associated with MMS 10, and (2) the morphology of the blueshifted lobe seems to become more collimated toward the position of the 24  $\mu$ m source, but not toward MMS 10. A NIR reflection nebula elongated in the same direction as the blueshifted outflow is detected to the northeast of the 24  $\mu$ m source, as denoted by [13] in Figure 6a, which supports the idea that the blueshifted outflow is driven by the 24  $\mu$ m source. Note that the redshifted emission southwest of the 24  $\mu$ m source could partially be a counterpart of the blueshifted outflow. It is, however, difficult for us to conclude this, because of the contamination by another nearby outflow associated with FIR 2 (see below).

**FIR 1b (probable).**—A redshifted CO(3–2) outflow is located southeast of FIR 1b, denoted by [iv] in Figure 6b, whereas weak extended blueshifted emission is northwest of FIR 1b. This extended blueshifted component may be the counterpart of the redshifted lobe, forming a bipolar outflow, as suggested by the previous CO(1–0) observations (Aso et al. 2000; Williams et al. 2003). This is, however, difficult to conclude because the blueshifted emission is less localized and also is connected to the prominent outflow associated with MMS 9. The redshifted outflow is probably associated with FIR 1b although we cannot rule out its possible association with FIR 1a. Note that neither FIR 1b nor FIR 1a is associated with any 24  $\mu$ m emission, preventing us from identifying the driving source of the outflow. There is no apparent outflow associated with FIR 1c.

**FIR 2 (clear).**—There is a clear bipolar CO outflow associated with FIR 2, centered on the 24  $\mu$ m source of SP 053524-050830, as shown in Figure 6b or 8b. This outflow has also been identified in CO(1–0) (Aso et al. 2000; Williams et al. 2003). The blueshifted emission is located to the southwest and the redshifted emission to the northeast of 24  $\mu$ m source.

**FIR 3 (clear).**—Red- and blueshifted CO(3–2) emissions elongated along the northeast to the southwest direction is seen in Figure 8b. Each of the emissions overlapping with the other has two peaks, and a prominent 24  $\mu$ m source, SP 053528-050935 associated with FIR 3, is located between the two peaks. This suggests that the outflow is driven by this 24  $\mu$ m source. This outflow was also identified in CO(1–0) and CO(2–1) (Aso et al. 2000; Williams et al. 2003; Wu et al. 2005). Because the blue- and redshifted lobes overlap, the axis of the outflow is considered to be almost on the plane of the sky. This geometrical configuration is also suggested by the position-velocity diagram cutting along the outflow axis showing “butterfly” like velocity structure. Our *JHK<sub>s</sub>* image presented in Figure 8a denoted as [14], shows bright knots and shell-like features to the northeast of FIR 3 and a reflection nebula to the southwest of FIR 3. These NIR features, which are associated with the CO(3–2) outflow, also support the idea that the outflow is driven by the 24  $\mu$ m source associated with FIR 3.

In the vicinity of the peak position of FIR 3, there is another 24  $\mu$ m source, SP 053527-050923 (also identified as MIR 20 by Nielbock et al. 2003), located at 15'' northwest of FIR 3. Our *JHK<sub>s</sub>* image presented in Figure 8a [15] shows a jetlike feature elongated to the west of this 24  $\mu$ m source. Interestingly, we also detected slightly extended blueshifted CO(3–2) emission coincident with the NIR jetlike feature (see Fig. 8b), even though it is difficult for us to clearly distinguish this blueshifted emission from the prominent blueshifted outflow driven by SP 053528-050935.

**FIR 4 (marginal).**—The strong millimeter source FIR 4 associated with a free-free jet, VLA 12, is in the near neighborhood of a 24  $\mu$ m source, SP 053527-051002. Although the CO(3–2)

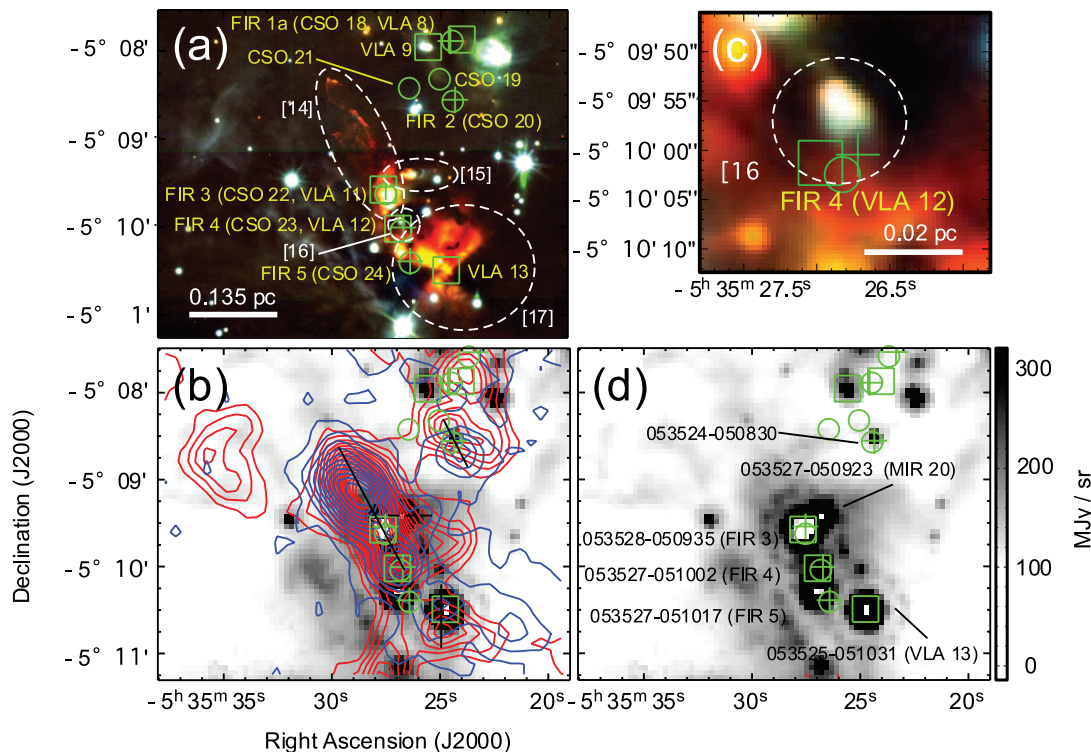


FIG. 8.—Images in the FIR 3–FIR 5 region. (a)  $JHK_s$  image taken by the IRSF/SIRIUS. (b) 24  $\mu\text{m}$  image taken with the *Spitzer* MIPS (gray scale) superposed on the CO(3–2) emission taken with the ASTE Telescope (contours). The blue and red contours show the blue- and redshifted components in the velocity range of  $-4.1 \text{ km s}^{-1} \leq V_{\text{LSR}} \leq 6.7 \text{ km s}^{-1}$  and  $14.3 \text{ km s}^{-1} \leq V_{\text{LSR}} \leq 21.9 \text{ km s}^{-1}$ , respectively. Blue- and red-contour intervals are  $8.40 \text{ K km s}^{-1}$  starting at  $5.04 \text{ K km s}^{-1}$  and  $4.62 \text{ K km s}^{-1}$  starting at  $7.70 \text{ K km s}^{-1}$ , respectively. (c) Zoom up view of the  $JHK_s$  image toward FIR 4. (d) The 24  $\mu\text{m}$  image taken with the *Spitzer* MIPS (gray scale) superposed on the source positions. Solid and dashed lines in panel b show the direction of the outflows categorized as clear (associated with FIR 2, FIR 3, and VLA 13) and probable (associated with MIR 20), respectively. Crosses, open circles, and open squares indicate positions of 1.3 mm, 350  $\mu\text{m}$  and 3.6 cm sources, respectively (from Chini et al. 1997; Lis et al. 1998; Reipurth et al. 1999). Dashed ellipses show the positions of NIR feature presented in Table 2.

line profile toward FIR 4 shows a broad wing, no clear CO outflow associated with FIR 4 was identified in our CO(3–2) map (see Fig. 8b). Millimeter interferometric observations also showed no clear outflow associated with FIR 4 (Shimajiri et al. 2008). This may be because there is strong contamination of the prominent outflow associated with FIR 3. In fact, we detected a faint NIR nebula in the vicinity of FIR 4, as denoted by [16] in Figures 8a and 7c, which could be a hint of a potential outflow associated with FIR 4.

**FIR 5(no).**—A 24  $\mu\text{m}$  source, SP 053527-051017 (corresponding to MIR 27 from Nielbock et al. 2003), is located at  $10''$  northeast of FIR 5. There is no clear bipolar CO lobe around this site.

**VLA 13 (clear).**—We detected a bipolar CO(3–2) outflow along the north-south direction centered on VLA 13, which coincides with a bright 24  $\mu\text{m}$  source, SP 053525-051031 (see Fig. 8b). Our  $JHK_s$  image shows that there is a bright cone-shaped  $K_s$  reflection nebula ([17] in Fig. 8a) coincident with this outflow.

**FIR 6a–FIR 6d.**—A bipolar CO(3–2) outflow categorized as “clear” lies northeast to southwest centered on FIR 6b (see Fig. 9b), which is associated with a 24  $\mu\text{m}$  source, SP 053523-051205 shown in Figure 9a. We also detected another bipolar CO(3–2) outflow running nearly north-south centered on FIR 6c. This outflow was also categorized as clear although its redshifted lobe might be partially the molecular ridge surrounding M43. No 24  $\mu\text{m}$  source is associated with FIR 6c. This might be because of a very high background level due to the emission from M43. Although FIR 6d is not associated with any clear CO(3–2) high-velocity lobe, a possible outflow we categorized as marginal was found at the position of FIR 6d as an NIR reflection nebula

denoted by [18] in Figure 9a. There is neither clear CO lobe nor NIR feature around FIR 6a.

**CSO 32 (marginal).**—although redshifted emission is associated with CSO 32, this redshifted emission appears to be a part of the molecular ridge surrounding M43.

**CSO 33 (probable).**—A blueshifted CO(3–2) emission associated with CSO 33 was detected as shown in Figure 9b. Our  $JHK_s$  image shows that a reflection nebula coincident with the blueshifted outflow was also detected. The reflection nebula extends to the east of CSO 33, which seems to be consistent with the elongation of the blueshifted emission. We cannot identify a driving source for this blueshifted outflow since there is no 24  $\mu\text{m}$  source associated with CSO 33. This may be because of the high background level due to M43. There is a redshifted emission located at  $15''$  east of CSO 33, and could be the counterpart of the blueshifted outflow. However, the direction of the redshifted emission is not consistent with the extension of the reflection nebula. In addition, the location of CSO 33 is not favorable for the interpretation of the redshifted emission as the counterpart of the blueshifted outflow. The redshifted emission may be a part of the molecular ridge surrounding and probably interacting with M43.

### 3.4. Notable NIR Sources

We have found three notable NIR sources in the OMC-2/3 region through the observations with SIRIUS/IRSF. Although these NIR sources are not associated with the 41 potential star-forming sites, the  $JHK_s$  images we obtained show probable star-forming activities.



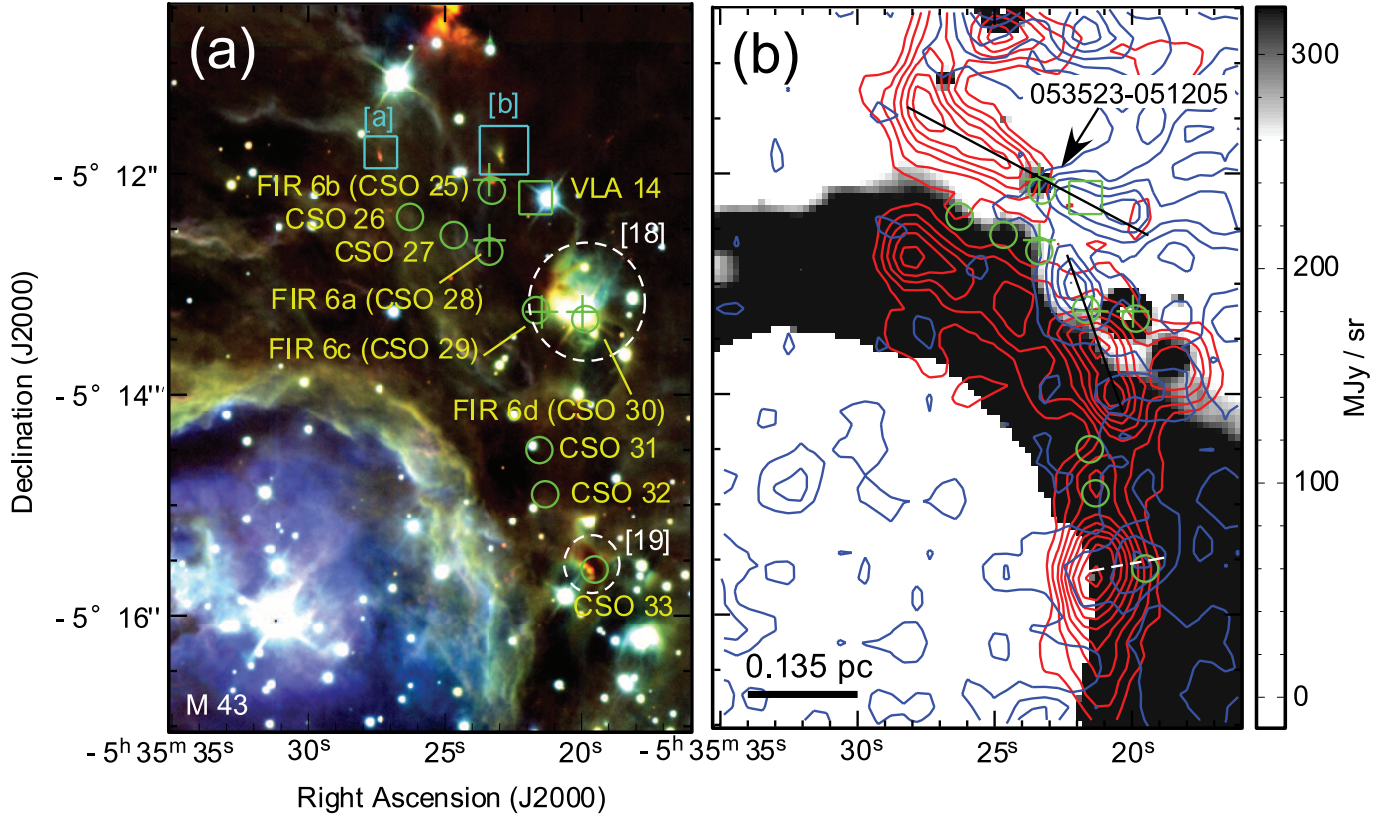


FIG. 9.—Images of the southern part of the OMC-2 region. (a)  $JHK_s$  image taken by the IRSF/SIRIUS. (b) 24  $\mu\text{m}$  image taken with the Spitzer MIPS (gray scale) superposed on the CO(3–2) emission taken with the ASTE Telescope (contours). The blue and red contours show the blue- and redshifted components in the velocity range of  $-3.9 \text{ km s}^{-1} \leq v_{\text{LSR}} \leq 6.7 \text{ km s}^{-1}$  and  $14.3 \text{ km s}^{-1} \leq v_{\text{LSR}} \leq 21.9 \text{ km s}^{-1}$ , respectively. Contour intervals are  $4.65 \text{ K km s}^{-1}$  starting at  $4.65 \text{ K km s}^{-1}$  and  $4.62 \text{ K km s}^{-1}$  starting at  $4.62 \text{ K km s}^{-1}$ , respectively. Solid and dashed lines in panel b show the outflows categorized as clear (associated with FIR 6 b) and probable (associated with FIR 6c and CSO 33), respectively. Crosses, open circles, and open squares indicate positions of 1.3 mm, 350  $\mu\text{m}$  and 3.6 cm sources, respectively (from Chini et al. 1997; Lis et al. 1998; Reipurth et al. 1999). Bright part at bottom left of panel a is M43. Dashed ellipse shows the position of NIR feature presented in Table 2.

The first source is a faint reflection nebula located at  $\sim 100''$  east of MMS 2 (denoted as [2] in Fig. 4a). This source was catalogued as 2MASS J05352454-0500214. Previous observations of  $\text{H}_2$  emission at 2.2  $\mu\text{m}$  suggested that this reflection nebula might be a knot related to the outflow from MMS 2 (Stanke et al. 2002). Our  $JHK_s$  image shows extended emission with a bright point source at the center of the emission (see Fig. 10a). The extended NIR emission appears as a cone-shaped structure due to an outflow with an axis nearly pole-on. These results suggest that the NIR feature probably traces an independent star-forming activity rather than a knot due to the outflow from MMS 2. Strong

blueshifted and faint redshifted CO(3–2) emissions were detected around this source (see Fig. 4b), but their relationship with the NIR feature is not clear.

The second source is a reddened pointlike source surrounded by an extended emission elongated from northeast to southwest (denoted as [a] in Fig. 9a). The source was catalogued as 2MASS J05352748-0511497. The size of the extended emission is  $\sim 8''$  (corresponding to 3600 AU) along the major axis, while  $\sim 4''$  (corresponding to 1800 AU) along the minor axis. Although there is no clear CO high-velocity emission associated with this source, the origin of the elongated feature might be an outflow cavity.

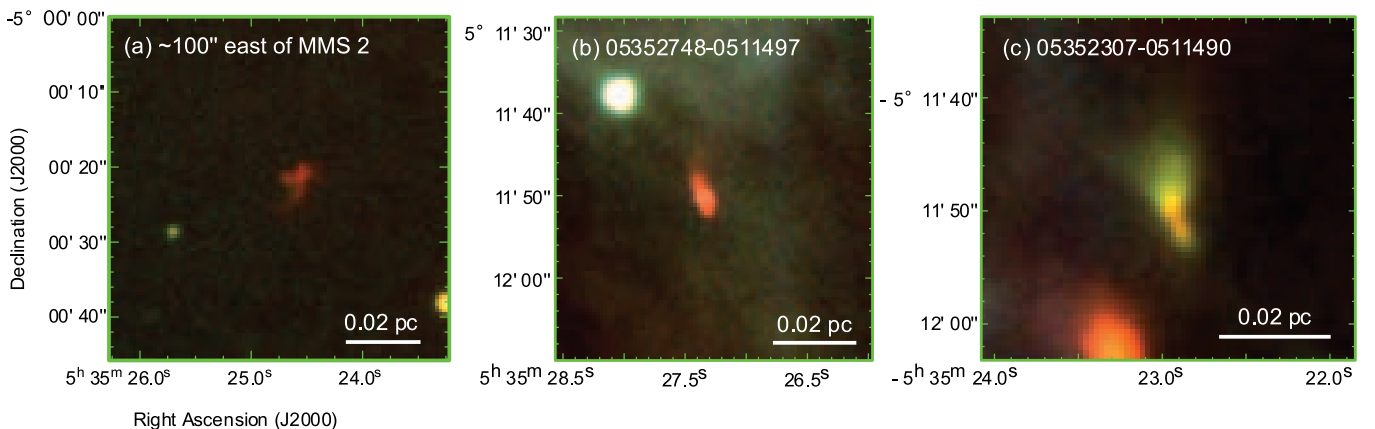


FIG. 10.— $JHK_s$  images of the extended NIR features taken by SIRIUS/IRSF. Pseudo colors of blue, green, and red show the data a J-, H-, and K- bands, respectively.

TABLE 3  
CO(3–2) OUTFLOW PARAMETERS

ID	Object name <sup>a</sup>	Criteria <sup>b</sup>	Inclination <sup>c</sup> (deg)	P.A. (deg)	Velocity Range (km s <sup>-1</sup> )	$\Delta V_{\max}^d$ (km s <sup>-1</sup> )	$R_{\max}^d$ (pc)	$M_{\text{CO}}^e$ ( $M_{\odot}$ )	$t_d^f$ (yr)	$\dot{M}_{\text{CO}}^f$ ( $M_{\odot} \text{ yr}^{-1}$ )	$F_{\text{CO}}^f$ ( $M_{\odot} \text{ km s}^{-1} \text{ yr}^{-1}$ )
Blue Lobe											
1.....	SIMBA <i>a</i>	C	45	50	7.8–8.9	4.7	1.2E-01	1.3E-03	2.5E+04	5.1E-08	3.4E-07
3.....	SIMBA <i>c</i>	P	45	...	8.9–10.0	3.6	1.0E-01	1.1E-02	2.7E+04	4.0E-07	2.0E-06
10.....	MMS 2	C	45	90	3.5–8.9	7.7	1.7E-01	6.9E-02	7.8E+03	8.8E-06	2.0E-04
13.....	MMS 5	C	45	–90	1.3–8.9	9.7	8.4E-02	4.0E-02	8.5E+03	4.7E-06	6.4E-05
16.....	MMS 7	C	70	90	4.6–8.9	6.0	1.5E-01	1.8E-02	8.9E+03	2.0E-06	3.5E-05
18.....	MMS 9	C	45	–100	–4.1–8.9	15.6	5.1E-01	4.7E-01	3.2E+04	1.5E-05	3.2E-04
20.....	VLA 9	P	45	40	2.4–8.9	9.4	3.7E-01	1.3E-01	3.8E+04	3.5E-06	4.6E-05
23.....	FIR 1 <i>b</i>	P	45	...	...	...	...	...	...	...	...
26.....	FIR 2	C	45	–150	–4.1–8.9	15.4	1.0E-01	3.2E-02	6.3E+03	5.1E-06	1.1E-04
28.....	FIR 3 (north)	C	70	30	–9.5–8.9	20.7	1.9E-01	1.3E-01	3.3E+03	3.9E-05	2.3E-03
28.....	FIR 3 (south)	C	70	30	–4.1–8.9	15.3	1.0E-01	4.8E-02	2.3E+03	2.1E-05	9.2E-04
30.....	VLA 13	C	45	0	2.4–8.9	8.8	8.4E-02	5.4E-02	9.3E+03	5.8E-06	7.2E-05
36.....	FIR 6 <i>b</i>	C	45	–115	1.3–8.9	9.0	1.7E-01	7.8E-02	1.8E+04	4.3E-06	5.4E-05
37.....	FIR 6 <i>c</i>	C	45	30	0.3–8.9	10.0	1.2E-01	2.0E-02	1.2E+04	1.7E-06	2.4E-05
41.....	CSO 33	P	45	...	3.5–8.9	7.2	8.4E-02	7.4E-02	1.1E+04	6.5E-06	6.6E-05
Red Lobe											
1.....	SIMBA <i>a</i>	C	45	50	13.2–16.5	4.0	1.4E-01	2.0E-02	3.4E+04	5.8E-07	3.3E-06
3.....	SIMBA <i>c</i>	P	45	...	...	...	...	...	...	...	...
10.....	MMS 2	C	45	90	13.2–16.5	5.3	1.5E-01	3.2E-02	7.6E+04	4.2E-07	2.4E-06
13.....	MMS 5	C	45	–90	13.2–21.9	10.9	1.0E-01	1.4E-02	9.0E+03	1.5E-06	2.3E-05
16.....	MMS 7	C	70	90	13.2–18.6	8.0	9.8E-01	1.4E-01	3.3E+05	4.4E-07	3.7E-06
18.....	MMS 9 (west)	C	45	–100	13.2–26.2	14.7	7.1E-01	2.8E-01	4.7E+04	6.0E-06	1.2E-04
18.....	MMS 9 (east)	C	45	–100	13.2–17.5	6.0	3.5E-01	4.9E-02	5.7E+04	8.6E-07	7.3E-06
20.....	VLA 9	P	45	40	...	...	...	...	...	...	...
23.....	FIR 1 <i>b</i>	P	45	...	13.2–17.5	6.2	8.4E-02	2.7E-02	1.3E+04	2.1E-06	1.8E-05
26.....	FIR 2	C	45	–150	13.2–20.8	9.5	6.8E-02	1.8E-02	7.0E+03	2.6E-06	3.4E-05
28.....	FIR 3 (north)	C	70	30	13.2–25.1	13.9	1.9E-01	9.7E-02	3.7E+04	2.7E-06	3.9E-05
28.....	FIR 3 (south)	C	70	30	13.2–22.9	11.7	1.0E-01	6.3E-02	2.3E+04	2.8E-06	3.4E-05
30.....	VLA 13	C	45	0	13.2–17.5	6.3	6.8E-02	1.4E-02	1.1E+04	1.3E-06	1.2E-05
36.....	FIR 6 <i>b</i>	C	45	–115	13.2–21.9	11.6	2.2E-01	4.9E-02	1.9E+04	2.7E-06	4.4E-05
37.....	FIR 6 <i>c</i>	C	45	30	13.2–19.7	9.4	1.8E-01	4.7E-02	1.9E+04	2.5E-06	3.4E-05
41.....	COS 33	P	45	...	...	...	...	...	...	...	...

<sup>a</sup> Object names in the column are from Chini et al. (1997), Lis et al. (1998), Nielbock et al. (2003), and Reipurth et al. (1999).

<sup>b</sup> C and P indicate outflows identified as clear and probable, respectively.

<sup>c</sup> Inclinations angles of MMS 2, MMS 7, and FIR 3 outflows were assumed nearly plane of the sky (i.e., 70°). Inclination of the other outflows were assumed 45°.

<sup>d</sup> Not corrected for inclination.

<sup>e</sup> H<sub>2</sub> mass of the CO outflow were derived by the LTE assumption. Here, the typical excitation temperature of CO(3–2) and the abundance were assumed to be  $T_{\text{ex}} = 30$  (see Fig. 11) and  $X[\text{CO}] = 10^{-4}$  (Frerking et al. 1982), respectively.

<sup>f</sup> Each parameter assumed inclination angle.

The last source is located at 80'' northwest of FIR 6*b* (denoted as [b] in Fig. 9*a*). The source, catalogued as 2MASS J05352307-0511490, has a cavity-like reflection nebula from nearly north to south, with a silhouette disk at its middle. Although there is no clear CO(3–2) high-velocity emission associated with the source, the cavity-like reflection nebula is suggestive of an outflow activity.

The possible origins of these NIR sources are low-mass protostars associated with low-mass molecular outflows with masses less than the detection limit of our survey.

#### 4. DATA ANALYSIS OF THE CO(3–2) EMISSION

Table 3 summarizes parameters toward 14 outflows categorized as clear or probable. Regarding the inclination angle of the outflows of MMS 2, MMS 7, and FIR 3, we assumed an inclination of 70°, since the outflow axes of these outflows are nearly on the plane of the sky as seen in the outflow morphology (i.e., blue- and redshifted lobes overlapping morphology) in the CO emission.

The inclination angle of the other outflows were assumed to be 45°. The projected maximum size of each CO(3–2) outflow was measured at the 3  $\sigma$  contour in its channel maps. The velocity range of each outflow was determined using channel maps: isolated components from high-velocity CO emission are clearly identifiable at more than 3  $\sigma$  level within the velocity range, without significant contamination of emission from the ambient component. The velocity ranges of the outflows were presented in the Table 3. The maximum velocity ( $\Delta V_{\max}$ ) of each outflow presented in Table 3 was calculated as  $|V_{\text{sys}} - V_{\max}|$ , where  $V_{\max}$  is either the most blueshifted or the most redshifted velocity of each outflow within its velocity range.

Under the assumption of the local thermodynamical equilibrium (LTE) condition and optically thin CO(3–2) emission, we estimated the outflow mass ( $M_{\text{CO}}$ ) as

$$M_{\text{CO}}[M_{\odot}] = \bar{\mu} m_{\text{H}} X[\text{CO}] \Omega_{\text{s}} D^2 N_{\text{CO}}, \quad (1)$$

where

$$N_{\text{CO}} \text{ (cm}^{-2}\text{)} = \frac{8\pi\nu^3}{c^3} \frac{1}{(2J_l + 3)A} \times \frac{Z(T_{\text{ex}})}{\exp(-E_l/kT_{\text{ex}})[1 - \exp(h\nu/kT_{\text{ex}})]} \times \frac{\int T_B dV}{J(T_{\text{ex}}) - J(T_{\text{bg}})}, \quad (2)$$

and

$$J(T) = \frac{h\nu/k}{\exp(h\nu/kT) - 1}. \quad (3)$$

In the above expressions,  $\bar{\mu}$  is the mean molecular weight of 2.33,  $m_{\text{H}}$  is the atomic hydrogen mass,  $h$  is Planck's constant,  $k$  is Boltzmann's constant,  $c$  is the speed of light,  $\nu$  is the line frequency,  $T_{\text{ex}}$  is the excitation temperature of the CO transitions,  $\Omega$  is a solid angle of each source,  $D$  is the distance to the objects,  $N_{\text{CO}}$  is the CO column density,  $T_{\text{bg}}$  is the background radiation temperature,  $A$  is the Einstein  $A$ -coefficient of the transition,  $Z$  is the partition function, and  $E_l$  is the rotational energy level of the lower energy state,  $J_l$  is the rotational quantum number of the lower energy state, and  $\int T_B dV$  is the integrated intensity of the blue- and redshifted CO(3–2) emissions in the unit of K km s<sup>−1</sup>. Each outflow emission was integrated using the velocity range of the CO(3–2) emission presented in Table 3. Here, we adopted  $T_{\text{ex}}$  of 30 K which is typical peak CO(3–2) brightness temperature in the OMC-2/3 filament (see CO line profiles in Fig. 11), and  $X[\text{CO}]$  of 10<sup>−4</sup> (e.g., Frerking et al. 1982). The detection limit of the mass corresponds to as small as 10<sup>−4</sup>  $M_{\odot}$  within a single beam.<sup>8</sup> The size and velocity of the outflow after the correction for the projection with the inclination angle,  $i$ , are estimated to be  $R = R_{\text{max}}/\sin i$ , and  $V = \Delta V_{\text{max}}/\cos i$ , respectively. Here, a pole-on outflow was defined as an inclination angle of 0°. We obtained the outflow dynamical time,  $t_d = R/V$ , mass outflow rate,  $\dot{M}_{\text{CO}} = M_{\text{CO}}/t_d$ , momentum,  $P_{\text{CO}} = \dot{M}_{\text{CO}} \times V_{\text{max}}$ , and momentum flux,  $F_{\text{CO}} = P_{\text{CO}}/t_d$ .

## 5. PROPERTIES OF THE PROTOSTELLAR CORES IN OMC-2/3

In Table 4 we list the derived physical properties of the individual protostellar cores having CO outflows categorized as clear. These individual sites have compact infrared sources (*IRAS* sources and/or *Spitzer* sources), which are considered to be the driving sources of the associated CO outflows. The bolometric luminosity of each driving source was estimated from the total flux density integrated from 8  $\mu\text{m}$  to 1.3 mm continuum data. Since the *IRAS* sources in these regions have only upper limits at 100  $\mu\text{m}$ , upper and lower limits of the bolometric luminosity for each driving source were derived with and without the flux density at 100  $\mu\text{m}$ , respectively. The mass of the envelope surrounding each of the driving sources was estimated from the 1.3 mm flux density observed by Chini et al. (1997) and Nielbock et al. (2003). On the assumption that the 1.3 mm continuum is optically thin, the mass is derived using the following formula:

$$M_{\text{dust}} = \frac{S_{\lambda} d^2}{\kappa_{\lambda} B_{\lambda}(T_{\text{dust}})}, \quad (4)$$

where  $\kappa_{\lambda}$  is the mass-absorption coefficient of the dust grains,  $B_{\lambda}$  is the Planck function,  $d$  is the distance to the OMC-2/3 region

(450 pc; Genzel & Stutzki 1989), and  $S_{\lambda}$  is the total flux density of the continuum emission within the 11'' radius (corresponding to 5000 AU) as repeated by Chini et al. 1997. We adopted a dust opacity of  $\kappa_{\nu} = 0.037 \text{ cm}^2 \text{ g}^{-1} (400 \mu\text{m}/\lambda)^{\beta}$  (Ohashi et al. 1996),  $\beta = 2$ , and  $T_{\text{dust}} = 20 \text{ K}$  (i.e., typical temperature of these cores from Cesaroni & Wilson 1994 and Chini et al. 1997). The estimated envelope masses are found to be  $\leq 1.0$  to  $7.7 M_{\odot}$ .

What is the evolutionary status of these sources? The spectral slope between near- and mid-infrared is often used to identify the evolutionary status of young stellar objects (e.g., Adams et al. 1988). We used the 2 and 10  $\mu\text{m}$  data taken by Nielbock et al. (2003) to derive spectral slopes of our 10 cores: 6 sources (MMS 2, MMS 7, FIR 2, FIR 3, VLA 13, and FIR 6b) were found to show positive slopes (e.g., rising spectrum toward 10  $\mu\text{m}$ ), suggesting that these sources are Class I type of objects. Four out of the 10 sources (SIMBA *a*, MMS 5, MMS 9, and FIR 6c), on the other hand, were not detected at 10  $\mu\text{m}$  and shorter wavelengths with the ground-based telescopes. Since these four sources are as luminous as the six detected sources mentioned above (see Table 4), they should not be too faint to be detected at 10  $\mu\text{m}$  and shorter wavelengths. A possible reason for this nondetection at near-infrared is that they are even more deeply embedded than the six detected sources. If this is the case, these four nondetected sources would be even younger than the six detected sources, i.e., Class 0 type of objects. Hence, these four sources are categorized as Class 0 type of objects in our paper. We note that the ratio of submillimeter luminosity ( $L_{\text{sub-mm}}$ ) to bolometric luminosity ( $L_{\text{bol}}$ ) is often used to distinguish Class 0 sources from Class I sources (Andre et al. 1993). It is, however, not easy for us to take this approach for our sample sources because of the large uncertainty of the bolometric luminosities we estimated, as described above.

## 6. DISCUSSION

### 6.1. Comparison with Previous CO(1–0) Observations

In addition to our CO(3–2) observations, outflow observations in the OMC-2/3 region were also conducted by Aso et al. (2000) with the Nobeyama 45 m telescope, and Williams et al. (2003) with the FCRAO 14 m telescope and the BIMA array. These previous observations were done in CO(1–0). In this section we compare our results with those obtained in the previous observations.

Out of 14 outflows (10 are categorized as clear and four are categorized as probable) we identified, the one associated with CSO 33 located in the most southern part of the OMC-2/3 region was not included in the previous outflow observations. Out of the rest, eight outflows associated with MMS 2, MMS 5, MMS 7, MMS 9, VLA 9, FIR 1b, FIR 2, and FIR 3 were also detected in both of the previous observations although one of them, associated with VLA 9, was considered to be associated with MMS 10 in the previous observations (see § 3.3.3; see also below). The physical parameters of these eight outflows derived from our CO(3–2) data (see Table 4) are roughly in agreement with those derived from the previous CO(1–0) data. On the other hand, five outflows associated with SIMBA *a*, SIMBA *c*, VLA 13, FIR 6b, and FIR 6c have been detected only in our CO(3–2) observations.

Why were these five outflows not detected in the previous CO(1–0) observations? One reason is the complexity of the region; some parts of the OMC-2 region form young stars as groups, and as a result, it is difficult for us to identify each outflow. For example, even though previous observations detected high-velocity redshifted CO(1–0) emission near VLA 13, it was not identified as an outflow associated with VLA 13. In this study, it was identified as an outflow associated with VLA 13 because of the near- and mid-IR data as well as the CO(3–2) data. A similar case is the

<sup>8</sup> We derived the detection limit of the outflow mass assuming that the 3  $\sigma$  emission level and  $\delta V = 1.08 \text{ km s}^{-1}$ .



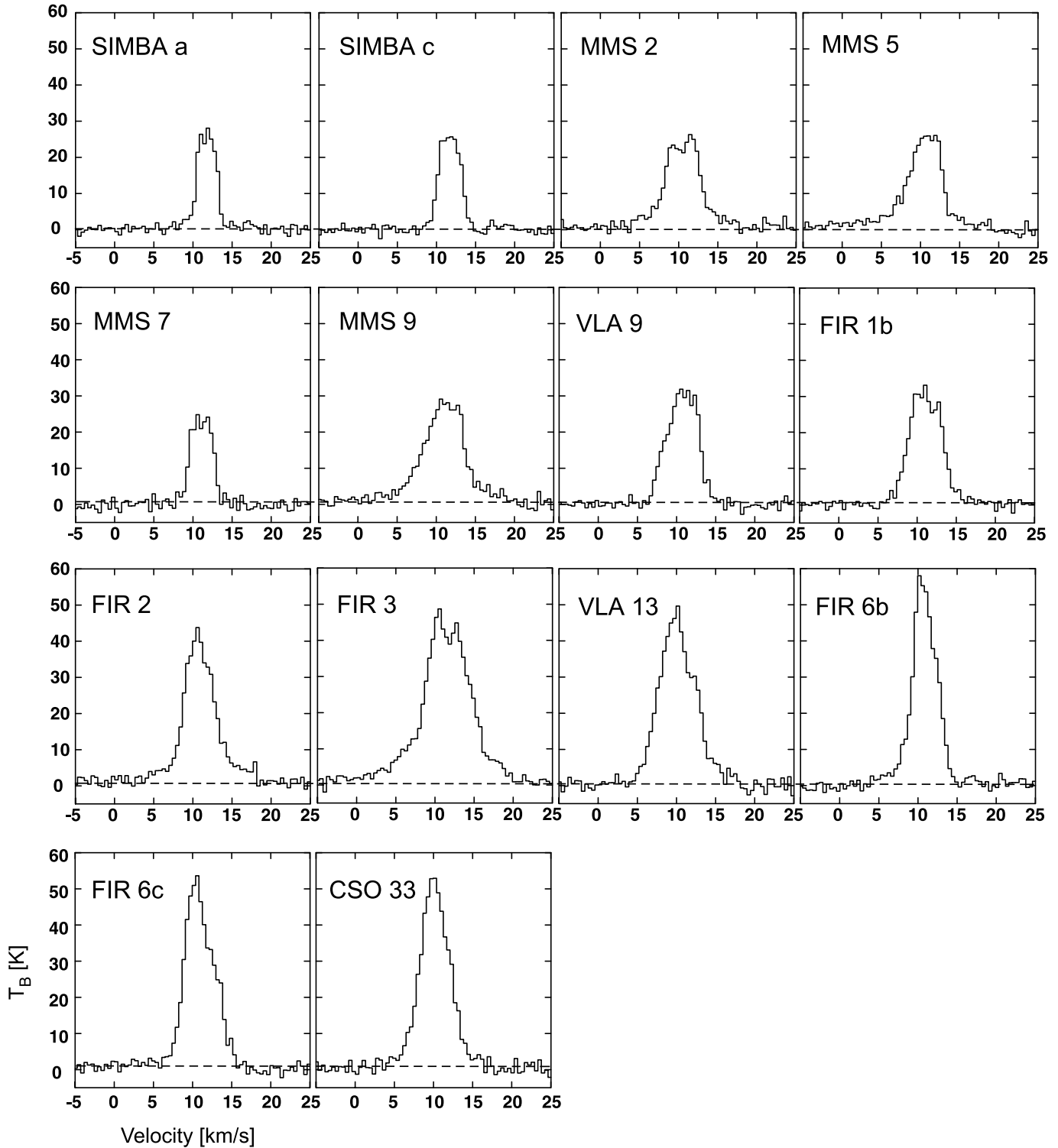


FIG. 11.—CO(3–2) spectra for clear and probable outflows in our sample at the positions of outflow driving sources (i.e., positions of 1.3 mm continuum sources or VLA 3.6 cm sources).

outflow associated with VLA 9; previous studies misidentified this outflow as that associated with MMS 10 because of the lack of near- and mid-infrared data.

Another possibility is that high-velocity emission is weaker in the CO(1–0). In the case of outflows associated with SIMBA *a* and SIMBA *c*, no high-velocity emission was clearly detected in CO(1–0) in the previous observations. These outflows are weak even in the CO(3–2) emission. Similarly, outflows associated

with FIR 6 *b* and FIR 6 *c* are significantly weak in CO(1–0) even though they are quite strong in CO(3–2).

Are outflow emissions systematically weaker in CO(1–0) as compared with CO(3–2)? In order to examine this, we compared the intensity of CO(1–0) and (3–2) emissions toward the outflow lobes. For this comparison, we used new CO(1–0) outflow maps of the OMC-2/3 region, recently taken using the Nobeyama 45 m telescope with the OTF mode (Kawabe et al.) in addition to our

TABLE 4  
PHYSICAL PROPERTIES OF THE POSSIBLE OUTFLOW DRIVING SOURCES

ID	Object Name	$L_{\text{bol. (min.)}}^{\text{ab}}$ ( $L_{\odot}$ )	$L_{\text{bol. (max.)}}^{\text{ac}}$ ( $L_{\odot}$ )	$M_{\text{env}}^{\text{d}}$ ( $M_{\odot}$ )	<i>Spitzer</i> 24 $\mu\text{m}$	<i>IRAS</i>	Classification <sup>e</sup>
1.....	SIMBA <i>a</i> <sup>f</sup>	5.6	...	6.5	053530-045848	...	0
10.....	MMS 2	14	150	2.8	053518-050034	...	I
13.....	MMS 5	9.0	...	4.5	053522-050115	...	0
16.....	MMS 7	71	99	4.1	053527-050355	05329–0505	I
18.....	MMS 9	60	155	4.7	053526-050546	...	0
26.....	FIR 2	59	217	3.9	053524-050831	...	I
28.....	FIR 3	30	300	7.7	053528-050935	...	I
30.....	VLA 13	24	286	$\leq 1.0$	053525-051031	...	I
36.....	FIR 6 <i>b</i>	6.0	251	3.4	053523-051205	...	I
37.....	FIR 6 <i>c</i>	<sup>g</sup>	...	5.1	...	...	0?

<sup>a</sup> The bolometric luminosity of each object is estimated from the total flux integrated by 8  $\mu\text{m}$  to 1.3 mm from Chini et al. 1997, Nielbock et al. 2003, and *Spitzer* archive data.

<sup>b</sup> Lower limit of the bolometric luminosity. (The data do not include *IRAS* 100  $\mu\text{m}$  upper limit fluxes).

<sup>c</sup> Upper limit of the bolometric luminosity. (The data include *IRAS* 100  $\mu\text{m}$  upper limit fluxes).

<sup>d</sup> Envelope mass were estimated by the flux within the diameter of 5000 AU (11'') by Chini et al. (1997).

<sup>e</sup> Evolutionary status of protostars were classified as Class 0 and Class I based on 2  $\mu\text{m}$  and 10  $\mu\text{m}$  results by Nielbock et al. (2003).

<sup>f</sup> The envelope mass of SIMBA *a* were estimated by the flux within the diameter of 10800 AU (24'') by Nielbock et al. (2003).

<sup>g</sup> The bolometric luminosity was not estimated due to negative detection of the near- to mid-infrared source.

CO(3–2) maps taken by ASTE. Since the CO(1–0) maps have a higher angular resolution (22'') than the CO(3–2) maps (26''), the CO(1–0) maps were convolved with a beam of 26''. For the outflows significantly detected in both CO(1–0) and (3–2), CO(3–2)/CO(1–0) intensity ratios were estimated to be 1–3, suggesting that CO(3–2) emission is at least comparable to, or brighter than CO(1–0) for the outflows in the OMC-2/3 region.

It is interesting to consider what kind of physical conditions could make the CO(3–2) emission a few times stronger than the CO(1–0) emission. With the Large Velocity Gradient (LVG) calculations (Goldreich & Kwan 1974), the CO(3–2)/CO(1–0) ratio would be more than unity when H<sub>2</sub> density range of  $1.5 \times 10^3$  to  $2 \times 10^4 \text{ cm}^{-3}$  and the kinematic temperature of 40 K. The gas kinetic temperature at some of outflow lobes actually estimated to be more than 40 K from CO(3–2) line profiles. Hence, these molecular outflows we observed in the OMC-2/3 region probably have high-density gas of  $\sim 10^4 \text{ cm}^{-3}$ . Such high-density and high-temperature gas were found in the molecular outflow associated with L1157, one of the best-studied molecular outflows (Hirano & Taniguchi 2001).

## 6.2. Outflow Properties: OMC-2/3 Region versus Other Regions

In the following section we compare the physical nature of the outflows in the OMC-2/3 region with those found through previous systematic outflow searches in other star-forming regions. In order for us to minimize the ambiguity of the outflow identification, we limited our outflow sample in the OMC-2/3 region to those categorized as clear or probable in the §§ 6.2.1 and those categorized as clear in the § 6.2.2.

### 6.2.1. Detection Rate of the Outflows

Among the 41 potential star-forming sites listed in Table 1, 14 sites were found to be associated with CO outflows categorized as clear or probable. When we simply calculate the CO outflow detection rate using this result, the rate is 34%. On the other hand, previous outflow searches in low-mass star-forming regions (e.g., Bontemps et al. 1996; Hogerheijde et al. 1998) and in high-mass star-forming regions (e.g., Shepherd & Churchwell 1996; Zhang et al. 2001) showed that the detection rate is more than 80%. This might suggest that the CO outflow detection rate in the OMC-2/3 region is significantly lower than in the other star-forming re-

gions. We should note, however, that 23 of the 41 potential star-forming sites (49%) do not have *Spitzer* 24  $\mu\text{m}$  source; these sites are the so-called prestellar cores, where no infrared embedded sources have been found. In contrast, the previous outflow searches mentioned above were biased toward *IRAS* sources. When we limit our regions to those with 24  $\mu\text{m}$  sources, then the CO outflow detection rate becomes 67%. This is comparable to, but not as high as those of the previous searches. This is probably because (1) a part of the ambient molecular cloud in the OMC-2/3 region shows CO emissions with higher velocities, which are difficult to distinguish from molecular outflows; (2) some of the 24  $\mu\text{m}$  sources seem to be more evolved with less surrounding material.

### 6.2.2. Relation between Outflow Parameters and Driving Source Properties

Previous studies have discussed the driving mechanisms and the physical properties of CO outflows (e.g., Lada 1985; Cabrit & Bertout 1992; Bontemps et al. 1996). Their main conclusions are as follows: (1) CO molecular outflows driven by a highly collimated flow (i.e., primary jet) are observed as entrained surrounding molecular gas, (2) energy of each CO outflow is mainly determined by the luminosity of the central driving source, which is probably related to the processes of mass accretion onto the central stars. In this subsection we investigate the relationship between the physical parameters of the molecular outflows and of their driving sources.

In Figure 12 we plot the momentum flux of the outflow ( $F_{\text{CO}}$ ) as a function of the bolometric luminosity of the outflow driving source ( $L_{\text{bol}}$ ) for 10 sources from our sample. For comparison, Figure 12 also shows the data of 101 CO outflows associated with young stellar objects (YSOs) in low- and high-mass star-forming regions, which were previously observed in CO with single-dish telescopes (see Bontemps et al. [1996] and Hogerheijde et al. [1998] for low-mass star-forming regions, and Beuther et al. [2002] and Zhang et al. [2005] for high-mass star-forming regions).

Figure 12 clearly shows a positive correlation between  $F_{\text{CO}}$  and  $L_{\text{bol}}$ . The correlation is valid in a wide range of  $L_{\text{bol}}$  ( $0.1 \leq L_{\text{bol}} \leq 10^5 L_{\odot}$ ) and  $F_{\text{CO}}$  ( $10^{-6} \leq F_{\text{CO}} \leq 0.1 M_{\odot} \text{ km s}^{-1} \text{ yr}^{-1}$ ). Sources in low-mass star-forming regions have lower  $F_{\text{CO}}$  and  $L_{\text{bol}}$ , while those in high-mass star-forming regions have higher

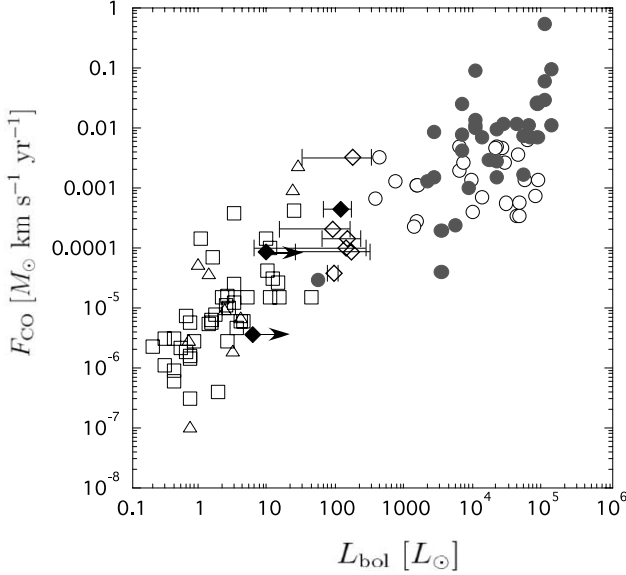


FIG. 12.—CO outflow momentum flux plotted as a function of the bolometric luminosity. Open and filled diamonds show Class I and Class 0 like protostars in the OMC-2/3 region (this work). Triangles, open squares, filled circles, and open circles show previous low- to high-mass survey results from Hogerheijde et al. (1998), Bontemps et al. (1996), Beuther et al. (2002), and Zhang et al. (2005), respectively.

$F_{\text{CO}}$  and  $L_{\text{bol}}$ . This conclusion has already been reported by Beuther et al. (2002). The sources in the OMC 2/3 region are located in this plot between the sources in low- and high-mass star-forming regions, and bridge a gap between them. The sources in the OMC-2/3 region have intermediate  $F_{\text{CO}}$  and  $L_{\text{bol}}$  in Figure 12, which naturally suggests that they are most probably intermediate-mass YSOs.

It is interesting to consider why both  $L_{\text{bol}}$  and  $F_{\text{CO}}$  can be good indicators of the mass of the YSOs. For low- and intermediate-mass YSOs, their bolometric luminosities are most probably dominated by the accretion luminosity ( $L_{\text{acc}} \equiv GM_*\dot{M}_{\text{acc}}/R_*$ ). If we assume that the stellar radius ( $R_*$ ) does not significantly change during protostellar evolution, the relation suggests that a higher  $L_{\text{bol}}$  indicates either a higher mass accretion rate or a higher central stellar mass, or both. Since a higher mass accretion rate results in a higher stellar mass as long as the mass accretion timescale is similar among low- and intermediate-mass protostars, it is fair to assume that  $L_{\text{bol}}$  is an indicator for the mass of YSO for low- and intermediate-mass YSOs. For high-mass YSOs, on the other hand, it is not always true that  $L_{\text{bol}}$  is dominated by the accretion luminosity since some of them reach the main sequence when they are still embedded in molecular clouds. If this is the case,  $L_{\text{bol}}$  is basically the same as the stellar luminosity, indicating that  $L_{\text{bol}}$  is an indicator of the stellar mass.

How about  $F_{\text{CO}}$ ? It is not very clear how  $F_{\text{CO}}$  can be an indicator of the mass of YSOs. Bontemps et al. (1996) suggested that  $F_{\text{CO}}$  has a linear relationship with the rate of mass accretion onto the central star for low-mass YSOs. This is because the most plausible energy source for a jet/wind, which is considered to drive a CO outflow, is the gravitational energy released by infall and/or accretion onto the central protostar. If this is valid for low- to high-mass YSOs,  $F_{\text{CO}}$  is indirectly related to the central stellar mass which is more or less determined by the mass accretion rate.

In Figure 13 we plot  $F_{\text{CO}}$  as a function of the envelope mass ( $M_{\text{env}}$ ). In the same way as in Figure 12, we plot sources in the low- and high-mass star-forming regions (Bontemps et al. 1996; Hogerheijde et al. 1998; Beuther et al. 2002), as well as those in

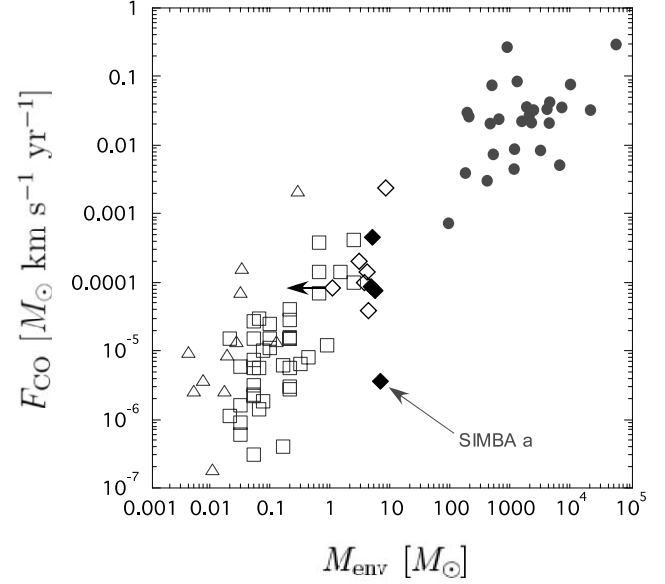


FIG. 13.—CO outflow momentum flux plotted as a function of the envelope mass. Open and filled diamonds show Class I and Class 0 like protostars in the OMC-2/3 region (this work). Triangles, open squares, and filled circles show previous low- to high-mass survey results from Hogerheijde et al. (1998), Bontemps et al. (1996), and Beuther et al. (2002), respectively.

the OMC-2/3 region. Figure 13 clearly shows a good correlation between  $F_{\text{CO}}$  and  $M_{\text{env}}$ . Note that Bontemps et al. (1996) also showed the same correlation for low-mass YSOs, whereas Figure 13 includes not only low-mass Class 0 and Class I sources, but also intermediate- and high-mass YSOs. Figure 13 shows that more massive YSOs are associated with higher envelope masses, suggesting that  $M_{\text{env}}$  is a good indicator of the YSO mass. This is probably not surprising because the core mass function often shows a relation similar to the initial mass function in various star-forming regions (e.g., Testi & Sargent 1998; Motte et al. 1998; Nutter & Ward-Thompson 2007).

As discussed above, our sample sources are considered to be intermediate-mass YSOs. In the OMC2/3 region, however, low-mass YSOs should form as well (see § 3.4). Why are no low-mass YSOs included in our sample sources? One probable reason is that our sample sources are selected based on 1.3 mm, 350  $\mu\text{m}$ , and 3.6 cm observations, as described in § 3.1. The mass sensitivity ( $3\sigma$ ) of the dusty envelope detected in the 1.3 mm observations is roughly  $1 M_{\odot}$ . For comparison, a typical value of the envelope mass associated with low-mass protostars are 0.01 to  $1 M_{\odot}$  (e.g., Bontemps et al. 1996; Hogerheijde et al. 1998; see Fig. 13). Therefore, most low-mass candidates may have been missed in our sample sources. In other words, our observations were biased toward the intermediate-mass protostellar cores.

In addition to the discussion whether the outflow momentum flux depends on the central protostellar mass, it is also important to consider the evolutionary effect on the outflow momentum flux. Bontemps et al. (1996) found a decline in the CO momentum flux from the Class 0 to Class I phase, suggesting that the outflow power declines with age. This result would be related to the decline of the mass accretion rate during the protostellar evolution. Our observational results were also examined from this point of view. In Figures 12 and 13, Class I sources in our sample were plotted as open diamonds while Class 0-like sources in our sample were plotted as filled diamonds. Figures 12 and 13 show no clear difference in the distribution of the momentum flux between Class 0 and Class I source in our samples. Why was no evolutionary trend seen in our samples? One possible reason is that



the number of our sample sources may be too small to see such an evolutionary trend.

We should, however, note that there might be one example that shows a possible evolutionary trend. The source is SIMBA *a*, one of the Class 0-like sources in our sample. This source has particularly small momentum flux in comparison with the other sources in our sample, and seems not to follow the  $M_{\text{env}}-F_{\text{CO}}$  correlation in Figure 13. Even though  $M_{\text{env}}$  of SIMBA *a* is as massive as those of our other samples, its  $F_{\text{CO}}$ ,  $3.6 \times 10^{-6} M_{\odot} \text{ km s}^{-1} \text{ yr}^{-1}$ , is 1–2 orders of magnitude smaller than others. This source might be in the earliest stage of the protostellar evolution, in which the mass of the envelope is large whereas the accretion/outflow activity is still less.

## 7. SUMMARY

We have carried out an extensive outflow survey in the submillimeter CO(3–2) emission and at  $JHK_s$ -bands toward the Orion Molecular Cloud 2 and 3 region which includes 41 potential star-forming sites. Main results are summarized as follows:

1. From CO(3–2) and  $JHK_s$  observations in addition to the multiwavelength continuum data, we detected 14 secure outflows, a half of which are newly identified in the OMC-2/3 region. We also found *Spitzer* 24  $\mu\text{m}$  sources toward 12 out of the 14 outflows as their driving source. In addition to these CO outflows, seven sources having NIR features suggestive of outflows were identified. This high fraction of newly identified CO outflows suggests that CO(3–2) emission may be a better outflow tracer than CO(1–0).
2. The outflow detection rate in OMC-2/3 is 34%, which is significantly lower than those in previous low- and high-mass

studies (i.e.,  $\geq 80\%$ ). This is because the 41 potential star-forming sites probably include 23 potential prestellar cores. When we limit our sample to those with 24  $\mu\text{m}$  sources, the CO outflow detection rate becomes 67% which is comparable to the previous low- and high-mass outflow studies.

3. Physical properties of these outflows and their possible driving sources were derived. Our results bridge a gap between previous low- and high-mass outflows, and the derived parameters show  $L_{\text{bol}}-F_{\text{CO}}$  and  $M_{\text{env}}-F_{\text{CO}}$  tight correlations regardless of the mass of the driving source. These results naturally suggest that the detected outflows in the OMC-2/3 region most probably are driven by intermediate-mass protostars.

The authors are grateful to T. Sawada, and K. Nakanishi for their support during the ASTE observations. We acknowledge A. Ishihara and SIRIUS/IRSF team for supporting the SIRIUS/IRSF observations. We also acknowledge P. T. P. Ho, Hsieh P., Y-N. Su, K. Saigo, J. Karr, and M. Puravankara for fruitful comments. This publication used archival data from the *Spitzer Space Telescope*. We thank D. Johnstone and D. Lis for providing us the submillimeter continuum data taken by JCMT and CSO, respectively. We also thank the referee for the constructive comments that have helped to improve this manuscript. A part of this study was financially supported by the MEXT Grant-in-Aid for Scientific Research on Priority Areas No. 15071202 and No. 16077204. S. Takahashi was financially supported by the Japan Society for the Promotion of Science (JSPS) for Young Scientists.

## REFERENCES

- Adams, F. C., Lada, C. J., & Shu, F. H. 1988, *ApJ*, 326, 865  
 Andre, P., Ward-thompson, D., & Barsony, M. 1993, *ApJ*, 406, 122  
 Arce, H. G., Shepherd, D., Gueth, F., Lee, C.-F., Bachiller, R., Rosen, A., & Beuther, H. 2007, *Protostars and Planets V* (Tucson: Univ. Arizona Press), 245  
 Aso, Y., Tatsumatsu, K., Sekimoto, Y., Nakano, T., Umemoto, T., Koyama, K., & Yamamoto, S. 2000, *ApJS*, 131, 465  
 Bachiller, R., & Tafalla, M. 1999, in *The Origin of Stars and Planetary Systems*, ed. C. J. Lada and N. D. Kylafis (Dordrecht: Kluwer), 227  
 Beltrán, M. T., Estalella, R., Girart, J. M., Ho, P. T. P., & Anglada, G., 2008, *A&A*, 481, 93  
 Beltrán, M. T., Girart, J. M., & Estalella, R. 2006, *A&A*, 457, 865  
 Beuther, H., Schilke, P., Sridharan, T. K., Menten, K. M., Walmsley, C. M., & Wyrowski, F. 2002, *A&A*, 383, 892  
 Bontemps, S., Andre, P., Terebey, S., & Cabrit, S. 1996, *A&A*, 311, 858  
 Cabrit, S., & Bertout, C. 1992, *A&A*, 261, 274  
 Cesaroni, R., & Wilson, T. L. 1994, *A&A*, 281, 209  
 Chini, R., Ward-Thompson, D., Bally, J., Nyman, L.-Å., Sievers, A., & Billawala, Y. 1997, *ApJ*, 474, L135  
 Churchwell, E. 1997, *ApJ*, 479, L59  
 Emerson, D. T., & Graeve, R. 1988, *A&A*, 190, 353  
 Ezawa, H., Kawabe, R., Kohno, K., & Yamamoto, S. 2004, *Proc. SPIE*, 5489, 763  
 Frerking, M., Langer, W. D., & Wilson, R. W. 1982, *ApJ*, 262, 590  
 Fuente, A., Neri, R., & Caselli, P. 2005, *A&A*, 444, 481  
 Genzel, R., & Stutzki, J. 1989, *ARA&A*, 27, 41  
 Goldreich, P., & Kwan, J. 1974, *ApJ*, 189, 441  
 Haro, G. 1953, *ApJ*, 117, 73  
 Hirano, N., & Taniguchi, Y. 2001, *ApJ*, 550, L219  
 Hogerheijde, M. R., van Dishoeck, E. F., Blake, G. A., & van Langevelde, H., J. 1998, *ApJ*, 502, 315  
 Johnstone, D., & Bally, J. 1999, *ApJ*, 510, L49  
 Kamazaki, T., et al. 2005, in *ASP Conference Ser. 347, Astronomical Data Analysis Software and Systems XIV*, ed. P. S. M. Britton & R. Ebert (San Francisco: ASP), 533  
 Kohno, K., et al. 2004, in *The Dense Interstellar Medium in Galaxies*, ed. S. Pflanzner, C. Kramer, C. Staubmeier, & A. Heithausen (Heidelberg: Springer), 349  
 Lada, C. J. 1985, *ARA&A*, 23, 267  
 Lada, C. J., & Lada, E. A. 2003, *ARA&A*, 41, 57  
 Lis, D. C., Serabyn, E., Keene, J., Dowell, C. D., Benford, D. J., Phillips, T. G., Hunter, T. R., & Wang, N. 1998, *ApJ*, 509, 299  
 Mangum, J., Emerson, D., & Greisen, E. 2007, *A&A*, 474, 679  
 Matthews, B. C., Lai, S.-P., & Willson, C. 2005, *ApJ*, 626, 959  
 Motte, T., Andre, P., & Neri, R. 1998, *A&A*, 336, 150  
 Nagashima, C., et al. in *Star Formation 1999*, ed. T. Nakamoto (Nobeyama: Nobeyama Radio Obs.), 397  
 Nagayama, T., et al. 2003, *Proc. SPIE*, 4841, 459  
 Nakajima, Y., et al. 2005, *AJ*, 129, 776  
 Nielbock, M., Chini, R., & Müller, S. A. H. 2003, *A&A*, 408, 245  
 Nutter, D., & Ward-Thompson, 2007, *MNRAS*, 374, 1413  
 Ohashi, N., Hayashi, M., Ho, P. T. P., Momose, M., & Hirano, N. 1996, *ApJ*, 466, 957  
 Reipurth, B., Bally, J., & Devine, D. 1997, *AJ*, 114, 2708  
 Reipurth, B., Rodriguea, L. F., & Chini, R. 1999, *AJ*, 118, 983  
 Reipurth, B., Rodriguea, L. F., Anglada, G., & Bally, J. 2004, *ApJS*, 127, 1736  
 Sawada, T., et al. 2008a, *PASJ*, 60, 445  
 Shepherd, D. S., & Churchwell, E. 1996, *ApJ*, 472, 225  
 Shimajiri, Y., Takahashi, S., Takakuwa, S., Saito, M., & Kawabe, R. 2008, *ApJ*, 638, 255  
 Stanke, T., McCaughrean, M. J., & Zinnecker, H. 2002, *A&A*, 392, 239  
 Takahashi, S., Saito, M., Takakuwa, S., & Kawabe, R. 2006, *ApJ*, 651, 933  
 Testi, L., & Sargent, A. I. 1998, *ApJ*, 508, L91  
 Tsujimoto, T., Koyama, K., Kobayashi, N., Saito, M., Tsuboi, Y., & Chandler, C. J. 2004, *PASJ*, 56, 341  
 Yu, K. C., Bally, J., & Devine, D. 1997, *ApJ*, 485, L45  
 Yu, K. C., Billawala, Y., Smith, M. D., Bally, J., & Butner, H. M. 2000, *AJ*, 120, 1974  
 Williams, J. P., Plambeck, R. L., & Heyer, M. H. 2003, *ApJ*, 591, 1025  
 Wu, Y., Zhang, Q., Chen, H., Yang, C., Wei, Y., & Ho, P. T. P. 2005, *AJ*, 129, 330  
 Zhang, Q., Hunter, T. R., Brenda, J., Sridharan, T. K., Molinari, S., Kramer, M. A., & Cesaroni, R. 2001, *ApJ*, 552, L167  
 Zhang, Q., Hunter, T. R., Brenda, J., Sridharan, T. K., Molinari, S., Wang, J., & Kramer, M. A., & 2005, *ApJ*, 625, 864